8 PAPER 3

RELATING 3D SURFACE DISPLACEMENT FROM SATELLITE- AND GROUND-BASED INSAR TO STRUCTURES AND GEOMORPHOLOGY OF THE JETTAN ROCKSLIDE, NORTHERN NORWAY

Harald Øverli Eriksen[1,2,*], Steffen G. Bergh[2], Yngvar Larsen[1], Ingrid Skrede[3], Lene Kristensen[3], Tom Rune Lauknes[1], Lars Harald Blikra[2,3], Halfdan Pascal Kierulf[4]

1 Norut, P.O. Box 6434, N-9294 Tromsø, Norway

2 Department of Geosciences, UiT-The Arctic University of Norway, P.O. Box 6050 Langnes, N-9037 Tromsø, Norway

3 Norwegian Water Resources and Energy Directorate, Vestre Rosten 81, N-7075 Tiller, Norway

4 Norwegian Mapping Authority, P.O. Box 600 Sentrum, N-3507 Hønefoss, Norway

* Correspondence: harald.overli.eriksen@norut.no; Tel.: +47-95935286

ABSTRACT

This study combines TerraSAR-X radar satellite data from ascending and descending orbits with ground-based radar (LiSALab) to calculate 3D displacement vectors for the Jettan rockslide, Troms, Northern Norway, classified as a high-risk object. Using calculated 3D displacement vectors, aspect data and strain rates in conjunction with structure, geomorphology, slope topography and borehole data of the unstable area, we identify zones undergoing displacement, e.g. extension/compression, displacement into or out of the slope and/or various degrees of tilting.

Our results show variable 3D displacement velocities, plunge and azimuth directions along strike from north to south, that segment the rockslide into distinct domains. In most places displacement patterns are structurally controlled, as spatial variation in azimuth and plunge of 3D displacement vectors can be related to variation in attitudes of the host rock fabrics, i.e. gneiss foliation, brittle faults and fractures. For example, 3D vectors azimuth directions are towards WNW and the plunge is shallower and spatially discontinuous in the northern part of the rockslide, compared to azimuth direction towards NW with steeper and spatially more continuous plunge in the south. Internally, the northern part of the rockslide consists of a complex graben system surrounded by orthogonal NW-SE and NE-SW trending ridges, scarps, terraces, depressions and crevasses, showing a repeated stepping 3D displacement pattern that may indicate complex fault geometry at depth with several stepped and discontinuous slide surfaces. Further, the 3D displacement vectors show displacement into the slope in the upper part and out of the slope in the lower parts of the northern area, which we interpret to be planar fractures becoming curved (listric) gliding surfaces towards depth, resulting in back-rotation of antithetic blocks. Correspondingly, 3D displacement velocities decrease downslope, possibly due to discontinuous sliding surfaces at depth, in combination with internal zones of compression, related to thrust stacking of blocks. Small-scale forward rotational movement in segmented domains of the rockslide possibly indicates ongoing toppling and tilting on adjacent planar sliding surfaces.

In the southern area N-S trending scarps, ridges and depressions arranged parallel to hillslope, and gently dipping terraces show a more homogenous displacement pattern. 3D displacement vectors show downslope increase in velocity and shallowing of plunge, indicating that displacement here is concentrated along hillslope parallel fracture sets and more continuous, planar fracture surfaces at depth. The data further suggest movement on listric faults at depth

giving back-rotation of blocks, thus creating inward extension, and local displacement out of the slope near the scarps.

We propose a structural-controlled slope displacement model including alternate planar and wedge failure along one or more of the orthogonal fracture sets in the unstable area, in addition to displacement along planar fractures curving to listric fractures at depth where they possibly also merge into gently downslope dipping foliation surfaces. Using the Jettan rockslide as a case study, we convincingly show how remote sensing data may contribute to examine structural and topographic control on rockslide kinematics, thus giving new insights into controlling subsurface geometry.

1 INTRODUCTION

Use of ground- and satellite-based radar for observation and monitoring of ongoing displacement combined with structural and geomorphological studies of e.g., complex rockslides, is an evolving field. The technique is used in a variety of applications, spanning from surveillance of human made structures and mines (Tarchi et al., 1999; Gourmelen et al., 2007; Pieraccini, 2013), monitoring of displacement patterns in natural processes like earthquakes, glacier flow (Goldstein et al., 1993), volcano deformation (Massonnet et al., 1995), subsidence (Strozzi et al., 2001; Chaussard et al., 2014) to rockslides/landslides (Berardino et al., 2003; Tarchi et al., 2003; Lauknes et al., 2010).

Both ground- and satellite-based radar instruments have proven to be reliable tools to measure displacement with main advantages including: (1) large spatial sampling and, (2) all-day all-weather capability, (3) possibility to observe displacement velocity ranging in scale from mm yr^{-1} to 10s m yr^{-1}.

However, remote sensing using single geometry radar datasets is limited to measure displacement in the instruments Line-Of-Sight (LOS) direction, while sensitivity to displacement in other directions is underestimated. If the direction of displacement is orthogonal to the instruments LOS-direction, the displacement will be invisible to the instrument. Several approaches have been proposed to increase sensitivity by combining overlapping displacement datasets. Techniques for resolving deformation in three dimensions (3D) for earthquakes and glaciers, such as azimuthal offsets (Fialko et al., 2001; Fialko et al., 2005) and offset tracking (Nagler et al., 2012) show good results for deformation in the order of decimeter to meter yr^{-1}.

Unfortunately, studies combining radar datasets having displacement in the order of mm yr^{-1} to cm yr^{-1} are limited due to, e.g. low availability of overlapping ground and satellite dataset in time and space. In this study, we combine ground- and satellite-based radar data to 3D displacement vectors for areas with velocity in the order of millimeters to centimeters yr^{-1}. For areas covered by the TerraSAR-X (TSX) satellite- (ascending and descending) and ground-based radar (LiSALab) campaign, we derive 3D vectors (magnitude and direction) for the Jettan rockslide, Troms, northern Norway.

This study attempts to gain new insight into the kinematics and movement patterns of the Jettan rockslide in Troms, northern Norway, using 3D vectors, and further, to discuss the possibilities and limitations by using 3D vectors for interpretation. We first compare 3D surface displacement vectors to mapped surface geological structures, slope and aspect directions of the topography, to examine overall structural and topographic control on rockslide kinematics and the interpreted, subsurface structural architecture. Then we investigate displacement patterns in more details along cross-sections, comparing kinematics in the northern and the southern part, and the upper and lower part of the rockslide. By using differences in combined 3D surface velocity, azimuth, plunge, slope dependency, aspect dependency and strain rate as diagnosing kinematic parameters we infer areas with displacement into and out of the slope, zones of compression and extension. 3D vectors are compared to a network of permanent global navigation satellite system receivers (GNSS) in the Jettan rockslide, making data applicable for resolving surface kinematics for landforms and deformation phenomena if covered by three or more individual radar datasets.

2 STUDY AREA

The Jettan rockslide covers an area of 0.9 km^2 from sea level to 800 m a.s.l., with a mean gradient of ~30˚ on the western side of the Nordnesfjellet on the Nordnes Peninsula in Troms County (Fig. 1), northern Norway. The Jettan rockslide has been classified as high-risk due to the severe consequences should a catastrophic failure occur, creating a tsunami in the nearby fjord system threatening the lives of thousands of people. The total volume of the currently active unstable area bounded by two active back-scarp fractures is c. 5-6 mill M^3 (Blikra et al., 2015). The rockslide has been extensively studied using multiple approaches including logging of boreholes cores (Ganerød, 2013, 2014), televiewer data (Elvebakk, 2013, 2014), ground- and satellite-based radar (Lauknes et al., 2010; Kristensen, 2011; Kristensen et al., 2011; Kristensen, 2013; Skrede, 2014), geophysical investigations (Tønnesen and Dalsegg, 2006; Rønning et al., 2008), geological mapping (Henderson et al., 2008; Blikra et al., 2009; Skrede, 2013), stability analysis (Nystad, 2014), interpretation of in-situ monitoring data (Nordvik et al., 2010), and study of ground thermal regime and deformation patterns (Blikra and Christiansen, 2014).

3 MATERIALS, METHODS AND DATA PROCESSING

3.1 TERRASAR-X INSAR PROCESSING

Using the Norut GSAR software (Larsen et al., 2005), snow-free scenes from 2009–2014 captured by the spaceborne TSX satellite in ascending and descending orbits were multi-looked, 6 × 6 and 8 × 6, respectively, processed to two stacks of interferograms, ~160 each, having a temporal baseline less than 55 days. The noise level in the interferograms was reduced using Goldstein filtering (Goldstein and Werner, 1998) and contribution from atmosphere filtered by estimating a phase delay elevation profile for each interferogram (Cavalié et al., 2007). The phase signal in each interferogram was unwrapped using the SNAPHU-unwrapper (Chen and Zebker, 2001), before manually removing interferograms having unwrapping errors. Assuming atmospheric contribution to be uncorrelated in time, interferograms from ascending and descending orbit were averaged (stacked) as described in Peltzer et al. (2001), producing two datasets showing phase mean difference based on all years observed from ascending and descending orbit. Finally, the ascending and descending mean phase datasets were converted to mean velocity (mm yr-1) and geocoded to 12x12 m resolution in map geometry using the 10 m DEM from NMA.

3.2 GROUND-BASED RADAR PROCESSING

Ground-based radar data were collected by NVE using an instrument from the Italian company Ellegi LiSALab s.r.l. Radar data were processed by Ellegi software (Ellegi srl, 2009: LISALab Technology: Methods and feasibility). The radar was located close to sea level below the rockslide, look up ~30°, scanning a sector from ENE to SE. NVE did a ground-based radar campaign from 07. May–17. September 2013 (133 days) with an acquisition each 8 minute. All images were processed and atmospheric noise removed. Then all images in five days intervals were statically processed to obtain one representative phase image free from atmospheric noise for every five days. The length of the five days interval was chosen by studying the movement seen in the radar images, as data wrapping does not occur in this time span. The entire dataset of representative phase images were then analyzed in order to provide displacement maps in the form of interferograms and cumulated images. Finally, accumulated displacement was geocoded on a DEM with a spatial of resolution of 1.2 x 1.2 m.

3.3 3D PROCESSING OF SATELLITE- AND GROUND-BASED RADAR

Based on the georeferenced ground-based radar dataset and position of radar we calculated the unit vectors for the ground-based radars LOS vectors for all pixels in the datasets. Further, we calculated the unit vectors for ascending and descending TSX datasets from radar geometry. With knowledge of magnitude along LOS for all three datasets, an inversion of a system with 3 linear equations with three unknown can be set up:

$$A * x = b$$

$$x = inv(A) * b \qquad \text{(Eq. 1)}$$

For each pixel in the common areas of the ground- and satellite-based radar displacement (input) dataset the resulting combined deformation vector x are calculated. A is a matrix representing the LOS unit vectors of the input datasets as columns, b a vector with deformation along LOS-direction for the input datasets, and x the resulting combined deformation vector in 3 dimensions.

We compared displacement patterns from 3D displacement vectors with GNSS-stations located in the rockslide area. We compute a mean yearly displacement vector for each GNNS station based on measurements for the same time period as covered by the TSX interferograms.

For combining ground and satellite datasets, an equal spatial resolution is needed. Equal spatial sampling was achieved by resampling of the fine resolution ground-based dataset (1.2 x 1.2 m) to the coarser resolution satellite dataset (12 x 12 m) using a nearest neighbor approach. InSAR measurements are relative, meaning that the dataset must be referenced to a known velocity for a point or area spatially covered. Usually an area assumed to be stable is used to calibrate the InSAR data. 3D processing demands that all in-datasets are equally referenced to a common area. However, we were unable to find a common stable area covered by all three in-data datasets. Therefore, we did a rough calibration of input data to the overall trend of GNSS network using the two-step calibration routine described in (Eriksen et al., 2017) before processing 3D displacement vectors. Lastly, we fine-tuned the calibrated InSAR data using an iterative workflow including (1) comparing GNSS displacement from the period covered by InSAR-data to averaged velocity, azimuth and plunge from displacement vectors originating from areas close to GNSS-stations 3, 5, 6 and 9, (2) recalibrating InSAR-input data and (3) 3D processing using recalibrated input data.

3.4 Geological, Structural and Geomorphological Data

In order to compare 3D displacement vectors and geological structures we used structural maps and field orientation data compiled by Skrede (2013) and Hernes (2014). To further investigate the relationship between displacement (kinematics), geological structures and geomorphology of the Jettan rockslide, we used 3D displacement vectors from a NNE-SSW reference longitudinal cross-section A–A' along-strike and parallel to hillside slope from north to south of the study area (Fig. 7 and Fig. 8). From this reference section, properties of the 3D surface displacement were plotted and discussed including velocity, azimuth, plunge, slope of topography and three values calculated from 3D displacement, displacement into or out of slope, aspect of the topography and its control of 3D displacement, and strain rate (downslope acceleration and deceleration). For comparison we investigated internal variations of 3D surface properties for the northern and southern part of the Jettan rockslide (Fig. 10). The same approach as in A–A' were used along two traverse cross-sections B–B' from ~450 to ~700 m a.s.l. using a 60 m buffer, and C–C' from ~430 to ~625 m a.s.l using a 130 m buffer. These cross-sections were used to discuss internal 3D displacements of the cross-sections and their relation to displacement recorded by GNSS-stations, mapped geological structures, geomorphology, slope and aspect of topography. Finally, we proposed geological models to explain the synthesized 3D displacement vector data.

3.5 Orthophotos and Digital Elevation Models

In addition, we used orthophotos (0.5 × 0.5 m and 1 × 1 m resolution), provided by Norwegian Mapping Authority (NMA) and aerial photographs provided by NVE, for more detailed interpretation of observed displacement patterns. We produced contour lines, topography slope maps, aspect maps and hill shade maps using a digital elevation model (DEM) based on LIDAR data from 2014 (1 × 1 m resolution) supplied by NMA. For areas not covered by the LIDAR DEM we used a 10 × 10 m resolution DEM (http://data.kartverket.no/download/content/digital-terrengmodell-10-m-utm-33) also from NMA.

3.6 GNSS

Displacement data from the GNSS-network at the Jettan rockslide were provided by NVE. We validate 3D vectors using GNSS data from four stations (Fig. 3) at the Jettan rockslide, by using a stable reference frame, data from the Norwegian Permanent GNSS network (Kierulf et al., 2014) were combined with GNSS-data from Jettan, as described in Eriksen et al. (2017). We computed the mean annual velocity vectors for GNSS-stations based on data from the same time interval (snow-free season from June to October 2009–2014) as covered by the interferograms in the TSX ascending and descending dataset (see Table 1 in (Eriksen et al., 2017).

4 RESULTS

4.1 3D DISPLACEMENT VECTORS COMPARED TO GNSS-NETWORK

After calibration, we compare 3D displacement vectors and GNSS-vectors, by plotting North-South, West-East and Up-Down components based on data from the same time-periods.

The largest deviations are in the north and height component (Fig. 4a, c). Especially the north component for the GNSS 3 area differ by having direction towards North (positive) in the 3D data and towards South (negative) in the GNSS-data (Fig. 4a), also resulting in some deviations in azimuth of the displacement (Fig. 4e).

The deviation between the annual GNSS displacement and the GNSS displacement from the time periods we focus on (snow-free season from June to October 2009–2014) due to seasonal variations are minor, and account for a difference of maximum 4 degrees in plunge of GNSS-vectors in the West-East Up-Down plane.

4.2 LOS-DIRECTIONS USED IN 3D INVERSION AND SENSITIVITY TO DISPLACEMENT

The orientation of LOS-vectors of the input data decides the reliability of the produced 3D vectors. The LOS-vectors for ascending and descending TSX data are constant over the rockslide, but the LOS-vectors of the ground-based radar vary (Fig. 5b). This variation results in variations in the LOS unit vector matrix A and the resulting vector 3D displacement vector x (Eq. 1). By calculating the condition numbers of the LOS unit vector matrix A, we get a relative quality estimate of the 3D displacement vectors. Condition numbers show how sensitive the resulting 3D displacement vectors (vector x in Eq. 1) are to variations in the input displacement data along the GB-radar, TSX ascending and descending LOS vectors (vector b in Eq. 1). The more parallel the LOS vectors of the input data are, the more numerically unstable (ill-conditioned) the 3D inversion will be, resulting in high condition numbers. Our results show that the condition number increases when the azimuth of the GB-radar LOS vector approaches the same azimuth direction as the plane span by the TSX ascending and descending LOS vectors (TSX LOS-plane) (Fig. 5a). The plunge of the GB-data LOS vector is relative stable, and therefore does not influence on condition numbers. The 3D vectors with the highest condition numbers are located in the north of the dataset, coinciding with the northernmost GNSS-station (GNSS 3) with most pronounced deviations in the north component (a and Fig. 5b).

4.3 GEOLOGY AND STRUCTURE OF THE JETTAN ROCKSLIDE

The study area consists of Caledonian bedrocks comprising well-foliated gneisses and intercalated marble and schists (see cliffs in Fig. 2c and Fig. 6b) (Zwaan, 1988), with an undulating foliation dipping on average, gently to the NW (i.e. downslope). The bedrock of the rockslide is underlain by a high frequency of brittle fault-fractures, and bounded by two main, orthogonal steep back-scarp fracture sets (Fig. 2a, Fig. 6c, Fig. 7, Fig. 9) trending ca. NE-SW (in south) and NW-SE (in north), respectively (Braathen et al., 2004; Skrede, 2013). Similar oriented, smaller orthogonal, steep and planar fracture sets are abundant throughout the rockslide (Fig. 6b), and especially below the NW-SE master back-scarp in the north, separating internal orthogonal or wedge-shape blocks. In addition, a subsidiary ca. N-S striking and steeply W-dipping fracture set (Fig. 9a), which is subparallel to the general hill slope, and numerous other fracture-related discontinuities occur in the unstable area (Fig. 9). In the north a dominant NW-SE striking back-scarp fracture and subsidiary NE-SW and N-S fractures make up oblique, wedge-shaped blocks, graben-like features and variably tilted fault blocks with internal, disintegrated materials, bounded by synthetic (oblique downslope) and antithetic (toward hillside) fractures/faults (Fig. 2b, c, Fig. 3, Fig. 6c, Fig. 9a-d). Fractures, foliation and scarps in the north all show an increased dip from top to downhill in the northern part (Fig. 3, Fig. 8, Fig. 12). In the southern area, a simpler geometry with gently downslope dipping foliation, cut steep by ENE-WSW and predominating hillside-parallel NNE-SSW fractures (Fig. 8, Fig. 9e, f). Scarps and foliation show a steepening in dip as in the northern part, contrary, dip of fractures have a shallower dip from top to bottom in the southern area (Fig. 8, Fig. 13). Notably, some fractures in the south have opened in an oblique manner, more in the southern than in the northern part of the fractures as documented by Skrede (2013) (see the large fracture above GNSS-station 4 in Fig. 8).

The rockslide at Jettan also comprises structurally related surficial geomorphological elements, e.g. gently downslope and inward dipping terraces underlain by modest dipping bedrock foliation, fracture-bounding scarps, trenches, gullies, and ridges (Fig. 3). In total, these features classify the area as an unstable, complex rock slide/field area (Braathen et al., 2004), thus providing a structural framework for interpreting the displacement pattern (see below).

4.4 Displacement Trends Versus Structure

Results from 3D processing show that displacement is highest in the upper and northernmost areas of the rockslide close to GNSS 3. Here, blocks in the graben-structure bonded by the NW-SE striking back-scarp and subsidiary NE-SW fractures, have a maximum velocity ~65 mm yr^{-1} (Fig. 3, Fig. 7, Fig. 8). 3D surface displacement vectors azimuth is towards WNW (280°) Fig. 7, Fig. 8, Fig. 10a), indicating that both NW-SE and NE-SW fractures to be contributing as controlling factors (Fig. 9, a-d).

In the southern area (Fig. 8), velocity is highest in the lower part, i.e. ~35 mm yr^{-1}, and ~25 mm yr^{-1} in the upper part. The azimuth of the 3D displacement vectors is fairly uniform and NW-directed (290°) in the southern areas. 3D displacement are orthogonal to NE-SW trending fractures and scarps (Fig. 9e, f), indicating a clear structural control on the displacement direction.

The general plunge for 3D displacement vectors for the Jettan rockslide show a pattern of uniform and steeper plunges in the southern area compared to more shallow and varied plunges in the northern area (Fig. 10b and inset histogram). In the north there is a downslope shallowing in plunge from the upper to the lower parts.

4.5 Displacement Trends Versus Topography and Geomorphology

We calculated the aspect of the topography and its relation to surface displacement by subtracting azimuth direction of 3D displacement vectors from aspect of the topography for each pixel (Fig. 10c). For the Jettan rockslide, there is a general pattern of 3D displacement azimuth trending more towards north than the aspect of the topography, given by more positive than negative values in Fig. 10c and inset histogram. Further, we observe about the same topographic control on displacement direction in the northern and the southern area, from the same variance in aspect dependency (Fig. 10c inset histogram). This means that azimuth directions of 3D vectors in both areas vary about equally with respect to the aspect of the topography.

4.6 Displacement Into and Out of the Slope

We determined areas where displacement is into and out the slope by subtracting plunge of displacement vectors from slope of topography. Our results show variable patterns both in north and south (Fig. 10d). Notably, the southern area has a larger continuous area of displacement into the slope. In the north plunge of 3D vectors vary more between into and out of the slope (Fig. 10d inset histogram).

4.7 3D Displacement From Longitudinal (North-South) and Transverse Cross-Sections

The maximum 3D displacement velocity values occur in the northern part of the Jettan rockslide (Fig. 8, Fig. 11a), while there is a gradual decrease in the velocity southward. A corresponding change in azimuth of 3D displacement vectors is observed, from dominantly W-directed (~275°) and with gentle and varied plunge and displacement patterns in the north (Fig. 11b, c), to fairly uniform NW-directed (~287°) and steeper 3D vectors in the south (Fig. 11b, c).

As observed in map-view (Fig. 8) the overall displacement velocity decreases from north to south in the reference longitudinal cross-section A–A' (red line in Fig. 11a), whereas, by contrast, internal variations in the northern and southern area show the opposite pattern with velocity increasing towards south (gray lines in Fig. 11a).

Azimuth direction of 3D displacement vectors vary from a north trend in the southern area to a south trend in the northern area, but internal opposite trends do exist (grey lines in Fig. 11b). Plunge of 3D displacement is steeper in the southern part than in the northern part of cross-section A–A', but also here an internal opposite trend do exist (grey lines in Fig. 11c).

5 Discussion

Below we first discuss reliability (validation) of the calculated 3D surface displacement datasets, then proceed with analyzing 3D data and their relation to structures and geomorphology in the Jettan rockslide, and finally, summarize all data, proposing a geological model.

5.1 Effect of Aligned LOS-Plane and LOS-Vectors

By comparing 3D displacement vectors and displacement data from the different GNSS stations in the Jettan rockslide, the most pronounced deviation between the two measurement techniques is shown for the north component in the area near GNSS station 3, while most of the other GNSS-stations display smaller deviations (Fig. 4a). This deviation may be due to intrinsic properties of the 3D-inversion in this area, e.g. the spatial alignment of LOS vectors of the input datasets yielding numerically unstable 3D inversions. The result is higher condition numbers in the northern parts than in the south, as shown in Section "Ground-Based Radar Processing" (Fig. 4a). Ill-conditioning of the 3D inversion in this area will affect the accuracy of the North-South component because this is the direction orthogonal to the ground-based LOS when parallel with the TSX ascending-descending LOS plane. The ill-conditioning of the 3D inversion does not necessarily affect the sensitivity in the West-East Up-Down plane (Fig. 4b). Contrary, the deviation in the 3D north-component observed for GNSS 3, is not found for GNSS station 9, even though it is located in the northern area (Fig. 4a), also with high condition numbers (Fig. 5). This deviation may be due to a difference in monitoring technique. While GNSS-station 3 recording displacement owing to a single block, radar data observe averaged displacement from 12 x 12 m areas. When comparing point measurement from GNSS stations located in a such a complex and highly fractured rockslide like in Jettan, spatially averaged measurements, one should expect some deviations (see (Eriksen et al., 2017)).

5.2 Effect of Steep Topography

The topography inside the rockslide at Jettan is undulating with repeated fracture-related scarps, ridges and gullies, and terraces underlain by gently dipping bedrock foliation (Fig. 3, Fig. 7, Fig. 8). 3D data can only be calculated for areas where the ground-based and the two satellite-based radar datasets overlap. Due to its position at almost sea level and undulating topography inside the rockslide, the ground-based radar limits these common areas to steeper parts of scarps and lowermost convex part of terraces. GNSS station 3 and 9 are located close to the edge of scarps with steep surface relief below (Fig. 3, Fig. 7). 3D data selected for comparison with these GNSS stations therefore capture the mean displacement from mostly blocks in steep topography, while the GNSS stations record point measurement of more gentle topography of terraces above the scarps. The height component may therefore be overestimated explaining the deviation between the two measurement techniques (Fig. 4c). Other implications of excess vertical movements for calculated 3D-vectors may be that they display higher velocity (Fig. 4d) and steeper plunge (Fig. 4f) than recorded by GNSS-stations. However, the effect of a deviating height component is not so severe for GNSS 5, because this station is not located on the edge of a scarp. Nevertheless, we find the 3D data acceptable for interpreting surface displacement, though some caution must be taken regarding higher condition numbers affecting the North-South component in the northern area, the difference in measuring technique due to spatial sampling (point versus area), and overrepresentation of sampling of steeper areas in the 3D data.

5.3 Effects of Temporal and Spatial Sampling

Spatial and temporal sampling of satellite-based radar datasets differ from the ground-based radar dataset used in the 3D-inversion. For example, InSAR processing of TSX satellite data is based on temporal sampling (acquisition) every 11 day from June to October 2009–2014, while the ground-based radar data are based on continuous acquisitions every 8 minute from 10. May –15. September 2013 (128 days) though only averages for every five days were used here. Previous data and results of in-situ instrumentation show that the deformation pattern at Jettan follows a repeated distinctive seasonal pattern (Blikra et al., 2015). They found an abrupt increase to high deformation in spring, lasting over summer, then a gradual reduction occurs after snow cover has established, and finally a reduction to almost no deformation during winter. Because of this annual repeated velocity signal, and that all three datasets are from the snow-free season, we assume the same mean annual velocity for the TSX data, as for the ground-based radar campaign, and thus consider the mean velocities to be comparable and suitable as input to the 3D inversion. However, the computed mean annual velocity for all three in-datasets are most likely overestimated, because they originate from the time period where in-situ instrumentation record the highest deformation in the repeated seasonal deformation pattern (Blikra and Christiansen, 2014). The difference in spatial sampling is resolved by down-sampling the ground-based radar dataset to the 10 x 10 m pixel size of the TSX data from the ascending and descending orbit.

5.4 3D SURFACE DISPLACEMENT DATA RELATED TO GEOLOGICAL STRUCTURES

By combining InSAR data from TSX ascending and descending satellite orbit to 2D InSAR displacement data, (Eriksen et al., 2017) divided the most active part of the Jettan rockslide into a northern, a southern and a upper part with different displacement patterns. These areas largely, seem to coincide with the mapped and interpreted structural domains that segment the rockslide (Skrede, 2013). In the following sections, we use 3D surface displacement vectors (Fig. 8 and Fig. 10) to investigate further differences in displacement patterns between the northern and southern, upper and lower areas, as well as internal variation. Finally, we compare and correlate 3D vector data (Fig. 8, Fig. 10) with geological structures (Fig. 9, Fig. 12, Fig. 13) and geomorphological elements (Fig. 3), using constructed geological cross-sections (see overview in Fig. 8, and cross-sections in Fig. 11 and Fig. 14). Velocity decreases from north to south in the longitudinal cross-section A–A' (Fig. 11, red line), and contrasting internal variation with increasing velocity towards south (Fig. 11a, gray lines), may be what have caused larger fracture in the southern area to move and open in an oblique manner as noted by Skrede (2013). The obtained variations in 3D displacement data along the cross-section A–A' (Fig. 11) showing repeated sets of internal variation, can be used to infer the presence of segmented (compartmentalized) domains of the Jettan rockslide.

The change in azimuth direction of 3D displacement vectors from a north trend in the southern area to a south trend in the northern area (Fig. 10a), is more prominent when plotted in a cross-section (Fig. 11b). The internal variations in azimuth direction in the southern area of cross-section A–A coincide with a trend in both velocity (grey line in Fig. 11a), and in plunge (grey line in Fig. 11c), indicating that 3D displacement vectors with azimuth directions towards north have steeper plunge, and higher velocity.

Steeper plunge towards south may be controlled by the vicinity of steeply west-dipping fractures, and/or combined NW-SE and NE-SW fractures, that may have acted as sliding surfaces there (Braathen et al., 2004).

In the changing terrace-slope-terrace topography of the northern area, the combined trends from the top and downhill includes a decrease in 3D surface displacement velocity (black stippled line in Fig. 14a), steeper plunge (black stippled line in Fig. 14c), transition from displacement into the slope to out of the slope (red colors in the upper part and green in the lower part of B–B' in Fig. 10d), and a transition in internal downslope velocity gradient (strain rate) from overall extension (positive) towards compression (Fig. 14g). These trends indicate surface extension and displacement into the slope in the upper part and surface compression and displacement out of the slope in the lower part the northern area. Further, these data support a change in surface structure, e.g. large and still ongoing displacement into the slope in the upper part where a major NW-SE back-scarp bounds a frontal graben structure with several NE-SW and NW-SE trending orthogonal depressions and blocks with excess toppling material (Fig. 2a-c, Fig. 3, Fig. 7). By contrast, the downhill area displays a much simpler structure with dominant NW-dipping ridge-parallel fracture sets. We interpret the reduced downslope velocity in the lower northern area to be an effect of more intact underlying bedrock working as a stabilizing structure, similar as proposed by Blikra and Christiansen (2014) for the area in the south near GNSS 7.

For the azimuth of the 3D vectors we observe a weak and variable trend from WNW in the upper part to NW-directed in the lower parts of cross-section B–B' (Fig. 14b). This change in azimuth values suggests a change in direction of displacement on different sliding surfaces, i.e. likely controlled by attitudes of fractures and/or foliation surfaces (Skrede (2013). Possibly a rotation of subsurface structures from the upper area to the lower area, as shown by stereoplot of fractures in loose blocks and scraps (Fig. 9c rotated to Fig. 9a, and Fig. 9d to Fig. 9b). For example, the more varied, WNW-directed displacement pattern in the upper part of cross-section B–B', may be explained by complex kinematic interaction in a graben zone between two orthogonal fracture sets. This fracture architecture would favor downslope wedge failure (Wyllie and Mah, 2004), i.e. slip along the line of intersection of the orthogonal fractures (Fig. 3, Fig. 7). A calculated approximately NNW-oriented and 40 degrees plunge of the intersection line in the northern area, based on the two dominant fracture sets there (Fig. 9c), showing some deviation from the WNW-directed displacement pattern. Thus failure mechanisms in addition to wedge failure must also be active in this area.

The aspect values of the topography (Fig. 10c) and their relation to surface displacement (aspect control) also vary from the upper part to the lower part of cross-section B–B' (black stippled line in Fig. 14f). The change from north-directed aspect control to south-directed, from the upper part to the lower part of cross-section B–B' (Fig. 14f), is the opposite trend compared to the azimuth of the 3D vectors (Fig. 14b), suggesting that, aspect of the topography has little influence on the 3D displacement. However, since condition numbers (see Fig. 5), describing 3D inversion quality, increase towards north in our dataset, they would affect the reliability of the 3D azimuth direction data. Therefore, caution must be made when interpreting azimuth of, and aspect dependency on 3D displacement in the northern area. In the southern area, the azimuth dependency of 3D displacement is lowest in the middle of cross-section C–C’, but there is no clear relationship between aspect of topography and azimuth of 3D displacement.

Furthermore, regarding aspect and topography, we observe internal downslope increase in displacement velocity in the northern area coinciding with similar sets of steeper topography (Fig. 14a; red lines), and a downslope steepening in plunge of 3D displacement vectors (Fig. 14c; red lines). Hence, slope of topography may be a controlling factor for displacement. On the other hand, by plotting dip of geological structures mapped by Skrede (2013) (Fig. 3) collected along the cross-section B–B’ in the northern part of the Jettan rockslide, the average dip of fractures, scarps and foliations increase downslope (Fig. 12). This trend of steeper dip is also recorded by GNSS-stations 2, 3 and 9. (Fig. 12). Therefore, we suggest a combined topographic and structural control on displacement in the northern area.

Furthermore, by subtracting dip of topography from plunge of 3D displacement vectors, we see variations of displacement into slope and out of slope taking place inside individual domains along cross-section B–B’ in the northern area. We interpret the internal change from out of slope to into slope in the middle and upper domains (red lines in Fig. 14e at 129–172 m and 238–296 m along B–B’) to be a forward rotational movement, possibly due to an ongoing toppling-process. The opposite trend is observed in the lower part of cross-section B–B’ (~43–90 m in Fig. 14e), could indicate compression due to stacking of blocks as in thrust-imbricated zones. Similar processes have been described for nearby rockslides at Nomedalstinden (Husby, 2011) and Nordmannviktinden (Braathen et al. (2004).

By comparison, the northern area comprises a high number of relatively small blocks of partly or fully disintegrated and variably NE- and SW-ward tilted or rotated fault blocks in a triangular-shaped zone in between the two merging NW-SE and NE-SW striking, orthogonal fracture sets (Fig. 2a, Fig. 3, Fig. 6a, Fig. 7). These observations are further supported by detailed mapping and calculations by Nystad (2014), showing that both toppling and wedge failure processes are possible in the northern area.

Seasonal variations in the water table at ~90 m depth in borehole 2 (Elvebakk, 2014) correspond with the varying surface deformations measured by in-situ surface deformation (Blikra and Christiansen, 2014). It is not clear whether variations in the water table influences displacement at depth.

By comparison, the southern area of the Jettan rockslide (Fig. 8; cross-section C–C') displays a much more continuous 3D displacement vector pattern. Notably, we observe only one set of downslope increasing velocity (Fig. 14a), and a corresponding steeper plunge of the 3D displacement vectors in the upper part, constant in the middle part and shallower plunge in the lower part of C–C' (Fig. 14c; curved trend). Structural orientation data for surface-related fractures along cross-section C–C' support the shallowing plunge of 3D displacement vector data from GNSS-stations (Fig. 13), i.e. verifying these structures acted as sliding/movement surfaces along the cross-section C–C'. Furthermore, field observations of back-rotated slide blocks (Eriksen (2013), several observations by Skrede (2013) of steep fractures becoming listric (curved) (Fig. 6b) and outcropping of two low-angle, foliation-parallel detatchments in the cliff face (Braathen et al. (2004), all indicate that that the same structures may be present at depth as well, and likely responsible for displacement patters observed by 3D vectors.

The southern areas of the unstable Jettan rockslide define a more coherent and intact bedrock structure than in the northern area. Foliation is gently (<30 degrees) dipping downslope, and cut by the dominant NNE-SSW striking brittle fracture set parallel to the hillside, and the subsidiary and ENE-SSW striking set (Fig. 6d). We interpret the 3D vector data yielding more uniform NW-movement pattern here to reflect a displacement pattern controlled by repeated sets of planar and/or listric slope-parallel back-rotated surfaces/discontinuities. When steep fractures cut through more gently dipping foliation surfaces, a step-vise structural pattern with gradually more back-rotated blocks (or foliation surfaces) at depth may appear cf. Braathen et al. (2004) (see example from outcrop in Fig. 6b) (Fig. 14). At some places displacement may follow antithetic fractures and possibly, back-rotated foliation into the hillside.

5.5 Subsurface Structure and Kinematics

Regarding subsurface displacement pattern of the Jettan rockslide, movements are likely more complex in the northern area than in the south, and include a combination of several mechanisms. DMS monitoring and borehole data show that most displacement is directed toward NW and takes place on surfaces located between 40 and 50 m depths in borehole 2 close to GNSS 3. Logging by televiewer suggests that this displacement is a result of interactions between heavily fractured zones trending NW-SE steeply dipping towards SW, and foliation dipping at ~55–75° mostly towards W (Elvebakk, 2014). Alternatively, displacement may be controlled by an interaction between the two orthogonal steeply SW-and NE-dipping fracture sets. If similar subsurface structures exist as those observed at the surface this would increase the probability of a wedge-failure collapse in this northern area.

In southern area, the most favorable sliding surfaces would be the ductile Caledonian foliation, alternatively, brittle NW- and/or SW dipping fractures that e.g. have become listric and merging into the foliation at depth (cf. Fig. 6b). From borehole 1 in the southern area such foliation-parallel fractures do occur at 20 to 40 m depth (azimuth towards W and plunge between 15-20°), together with a fracture-set dipping ~40° towards NW, documented by televiewer at ~45 m depth (Elvebakk, 2013). DMS data confirm that most of the deformation takes place at this depth (crushed zone) ~45 to 46 m with direction towards W (Blikra et al., 2015) (see red arrow at 45 m depth in borehole 1 in the southern area (Fig. 14). This is interpreted to be the main sliding surface in the upper part of the southern part of the Jettan rockslide. In the lower part of the southern area the main sliding surface is located deeper. Televiewer data from borehole 3 document foliation parallel West-dipping fractures from ~75–80 m depth (Elvebakk, 2014), DMS data show that highest cumulative deformation is taking place between ~77–87 m depth, congruent with a crushed zone at ~80 to 81 m (Ganerød, 2014). The downslope shallowing in plunge of 3D displacement vectors (Fig. 14c) is thought to be controlled by decrease in plunge of fractures as observed from the surface (green line in Fig. 13) and intersection lines between steeper fractures, and/or rotated structures due to listric fracture sets.

Allthough not documented in later measurements, an unexpected displacement pattern was recorded by the DMS-column in borehole 1 in the upper part of the southern area. Below 45 m depth, displacement direction is towards east (Blikra et al., 2015). This trend was very weak and inside the uncertainties, but it may be, as noted by (Nystad, 2014), an effect of back-rotation due to active movement along a listric (curved) fault/fracture at ~150 m depth (Elvebakk, 2013; Ganerød, 2013). We speculate that this could be a large scale version of antithetic movement along fractures and foliation as confirmed by observations on the surface (Fig. 6b) and discussed above. Such back-rotation of blocks and antithetic movement could create inward extension and produce local uplift near scarps, causing of the inferred uplift of the terrace above cross-section C–C’ as documented by Eriksen et al. (2017) using 2D InSAR.

Permafrost is not present in any boreholes, though, local patches of sporadic permafrost in deep fractures have been documented (Blikra and Christiansen, 2014). Therefore, some of the observed 3D surface displacement in the Jettan rockslide may originate from shallow deformation due to permafrost controlled rockslide deformation.

5.6 Rock-Slope Failure Model Based on Surface and Sub-Surface Structures

In a structurally controlled, complex field-type rockslide as in Jettan, various structural models may be applied to account for the 3D displacement data obtained, and local failure mechanisms can be proposed (cf. Braathen et al. (2004) and Wyllie and Mah (2004). The surface displacement signature of a deforming rockslide is the sum of all displacement taking place at depth. Usually sparse subsurface information about displacement patterns and geological structures make it hard to pose a reliable geological model. However, for the Jettan rockslide, 3D vector and surface geological data supplemented by data from boreholes, provide an important input for localizing tentative sliding surfaces at depth, and forms the basis for a tentative overall failure model for the northern and southern areas of the Jettan rockslide (Fig. 14h).

We favor a combined, “complex field” model (Braathen et al., 2004) for the unstable rockslide at Jettan by addressing (1) internal zones of extension in the upper northern part, with backward-rotational movements due to e.g. curved, listric and maybe discontinuous sliding surfaces at depth (cf. Rasmussen (2011), possibly combined with (2) internal zones of compression related to stacking of unstable, rotated blocks similar to that of thrust-imbricate zones (Braathen et al., 2004; Husby, 2011). In this tentative model for Jettan, the main orthogonal, NW-SE and NE-SW striking fractures, and corresponding smaller scale sets, define a fracture architecture that would favor downslope wedge failure collapse (Fig. 7) (Wyllie and Mah, 2004). This includes slip along the line of intersection of the orthogonal fractures, which is again closely perpendicular to the subsidiary NNE-SSW striking fractures. Such a scenario would favor the foliation as gliding surface, or alternatively, some of the steep planar fractures becoming listric toward depth (as observed in Fig. 6b), and/or when/if they merge into the gently NW-dipping foliation surfaces (see Fig. 14h). Such a change in subsurface structure may produce or be accompanied by inward rotation of antithetic blocks, thus creating inward extension, local uplift near the scarps, and compression in the downward section of the rockslide, due to buttress effects (see (Braathen et al. (2004); Blikra and Christiansen (2014))). 3D displacement confirm our model with a trend from displacement into the slope in the upper part to out of the slope in the lower part of both the northern part (cross-section B–B') and the southern part (cross-section C–C') (Fig. 14e). Listric faulting may be active both in large and small scale, as observed in the field as steep fractures curve to lower dip within meters (Fig. 6b), as they alternate between cutting and following foliation.

This model may apply for a "worst case scenario" estimated by Nystad (2014), i.e. if bedrock masses down to 45 m depth (5.5 - 6 million m^3) between the two main fracture scarps (Fig. 3, Fig. 7) move synchronously down slope. This mechanism may also account for possible smaller orthogonal-shaped blocks e.g. in the northern and central parts of area, where local and more varied movements patterns and a number of potential brittle fractures may be used as gliding surfaces (Fig. 3, Fig. 8, Fig. 10).

Another reliable model and accompanied displacement mechanism is planar-failure (Wyllie and Mah, 2004), i.e. inferred for the southern area, where one dominant NW-dipping back-scarp fracture set provides the controlling structure for downslope movement on e.g. west- to NW dipping, slope-parallel fractures, in conjunction with minor, transverse fractures perpendicular to them.

6 CONCLUSION

1) The use of remote sensing techniques to understand slope processes and controlling factors is a progressive evolving field. This paper shows how to combine three InSAR radar datasets to calculate 3D displacement vectors, and exploit 3D displacement properties such as velocity, azimuth, plunge and strain rate. 3D displacement properties are related to topography (displacement into or out of the slope and aspect), structure and geomorphology of the Jettan rockslide, Troms, northern Norway, where the deformation is in the order of mm to cm yr^{-1}.

2) We combine displacement patters and mechanisms by relating 3D displacement vectors and properties outlined above, in map view and cross-sections to displacement from GNSS-stations, host rock fabrics and borehole data. The 3D displacement data support the observed structural and geomorphological data in the Jettan rockslide and also, enable us to discuss displacement surfaces along host rock structural fabrics.

3) Movement pattern from 3D displacement vectors are different in the northern and southern parts of the Jettan rockslide. In the north, 3D vectors azimuth directions are towards WNW, and plunge is shallow and spatially discontinuous. In the south azimuth directions are toward NW, with steeper and spatially more continuous plunge. These data divide the rockslide into segmented domains.

4) In the northern area, the 3D vector attributes can be explained by the presence of a complex graben system. It is surrounded by orthogonal NW-SE and NE-SW trending ridges, scarps, terraces, depressions and crevasses, showing a repeated stepping 3D displacement pattern. This may indicate a complex fault geometry at depth, with several stepped and discontinuous sliding surfaces produced by the gently outward dipping foliation cut by steep fractures creating a step-wise attitude. Observed downslope decreasing velocity and increasing compression maybe related to stacking of blocks. Rotation of 3D vectors' azimuth from a WNW trend in the upper part to NW in the lower, is linked to change in azimuth of structures.

5) The displacements slope dependency, 3D vectors plunge compared to slope of terrain, suggest displacement into the slope in the upper part, and out of the slope in the lower, possibly as part of steep planar fractures becoming listric gliding surfaces towards depth. Where fractures merge into gently NW-dipping foliation surfaces, the resulting back-rotation of antithetic blocks give displacement inward along rotated foliation-parallel fractures.

Smaller internal variations in plunge (into and/or out of the slope) indicate forward rotational movement, possibly due to ongoing toppling.

6) In the southern area, 3D displacement vectors show downslope increase in velocity and shallowing of plunge, indicating that displacement here is concentrated along more continuous hillslope parallel fracture sets. NE-SW to NNE-SSW trending scarps, ridges and depressions arranged parallel to hillslope, and gently dipping terraces there support a more homogenous displacement pattern. The data further suggest movement on listric faults at depth giving back-rotation of blocks, possibly creating inward extension, and local uplift near the scarps.

7) We propose a structural-controlled slope displacement model including alternate planar- and wedge-failure collapse along one or more of the orthogonal fracture sets in the unstable area, that evolved from planar into curving (listric) fractures at depth, and where they possibly also merge into gently downslope dipping foliation surfaces, enhancing rotation of separate fault blocks.

8) Using the Jettan rockslide as a case study, we show how 3D displacement vectors from ground- and satellite-based InSAR data, may contribute to understanding structural and topographic control on rockslide kinematics, and ongoing displacement-failure processes. The approach used is applicable to study any displacement phenomena spatially and temporally covered by three radar datasets.

7 FIGURES

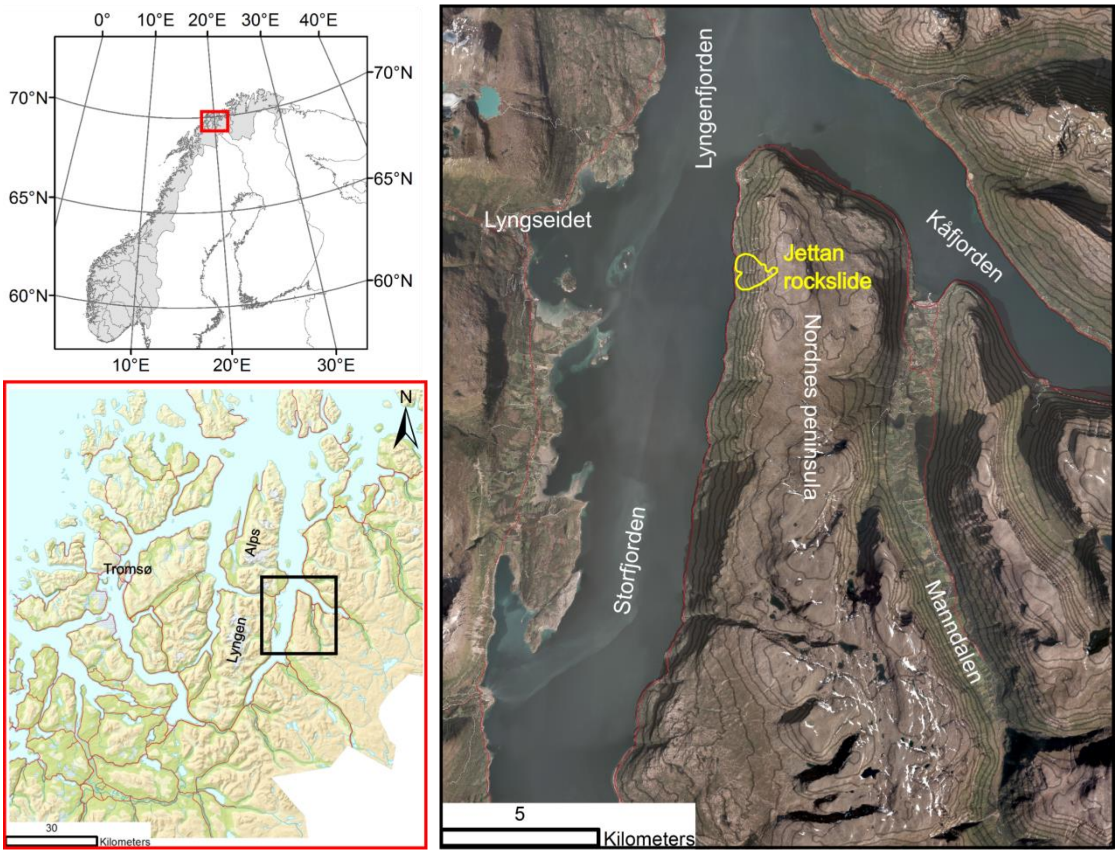

Fig. 1 – Location of the Jettan rockslide at the Nordnes Peninsula, in Troms County, northern Norway, east of the Lyngen peninsula. Contour interval is 100 m.

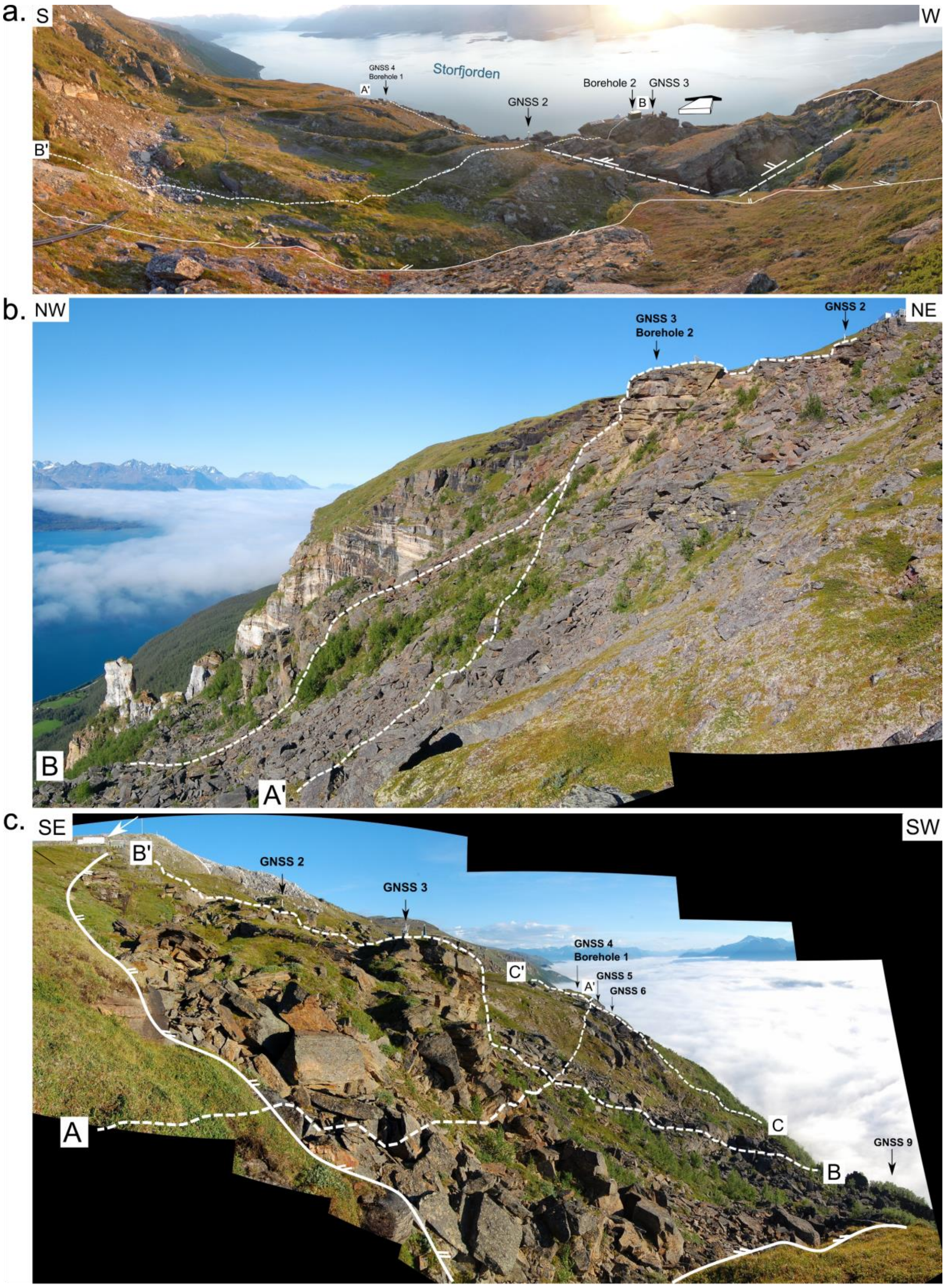

Fig. 2 – Overview of the Jettan rockslide with back scarp (white solid annotated line) separating stable from unstable bedrock and location of GNSS-stations and boreholes marked with black arrows. Cross-sections, or part of cross-sections, A–A', B–B' and C–C' are marked where they are visible. **a.** Outline of the complex graben system in the uppermost active part of northern area. Prominent SW and NW dipping fractures sets are marked. Note separate blocks of variably tilted bedrock, some moving outward and inward against the

master SW-dipping back-scarp (towards the hillslope in the far right of the photo. See also cliffs in the distance in Fig. 2c). A topographic terrace occurs to the left, with linear depressions marking fractures dipping NW, that are orthogonal to the back-scarp at the right. The entire wedge-shaped mass moves downslope toward WSW (large white arrow). GNSS station 3 and container with borehole instrumentation (DMS) for boreholes 2 are located on a large block in relief to the fjord, and GNSS station 2 just above. In the distance GNSS 4 and borehole 1 is visible. **b.** Overview of the chaotic northern area with graben structures in the upper part, and ongoing toppling from scarps. In the distance open NNE-SSW trending fractures are visible in the southern area. Note the ~8 m long white barrack above the back scarp in the northern area for scale, it is marked with a white arrow in the upper left corner. **c.** The slope-terrace-slope topography of the northern area with line of cross-section B–B', and transition from northern to southern area with line of cross-section A–A'. The well-foliated gneisses and intercalated marble and schists (white banded) NW-SE trending cliffs in the distance marks the northern extent of the rockslide

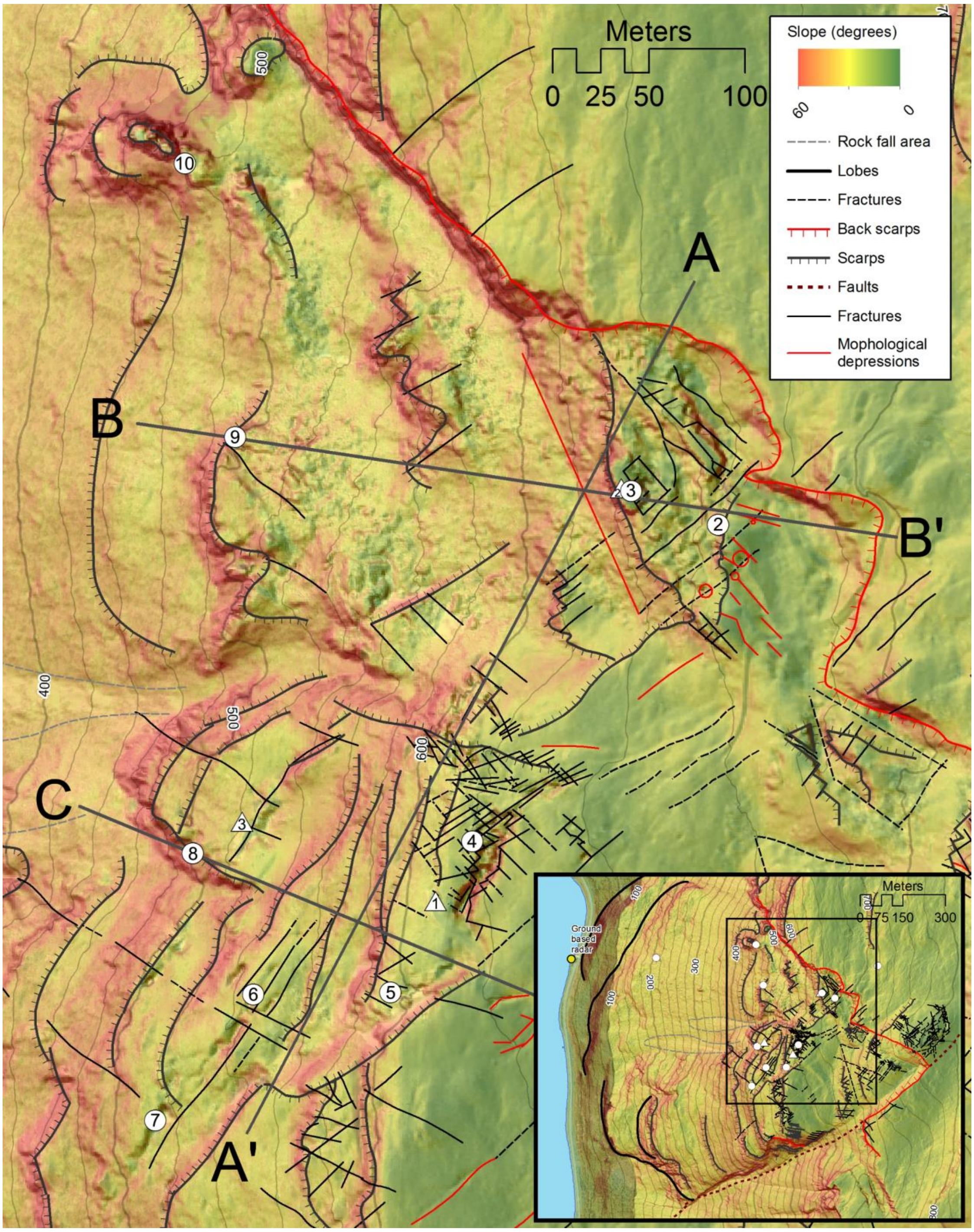

Fig. 3 – Hillslope map showing geological structures and geomorphological elements in the Jettan rockslide. The northern area is characterize by NW-SE and NE-SW trending orthogonal ridges, scarps, depressions and crevasses filled by disintegrated bedrock and block materials (cf. Fig 1b). In the southern area N-S to NE-SW trending scarps, ridges and depressions are arranged parallel to hillslope, bounding repeated sets of uniform terraces

dipping gently WSW. Map is modified from Skrede (2013). GNSS-stations marked with circles and boreholes with triangles.

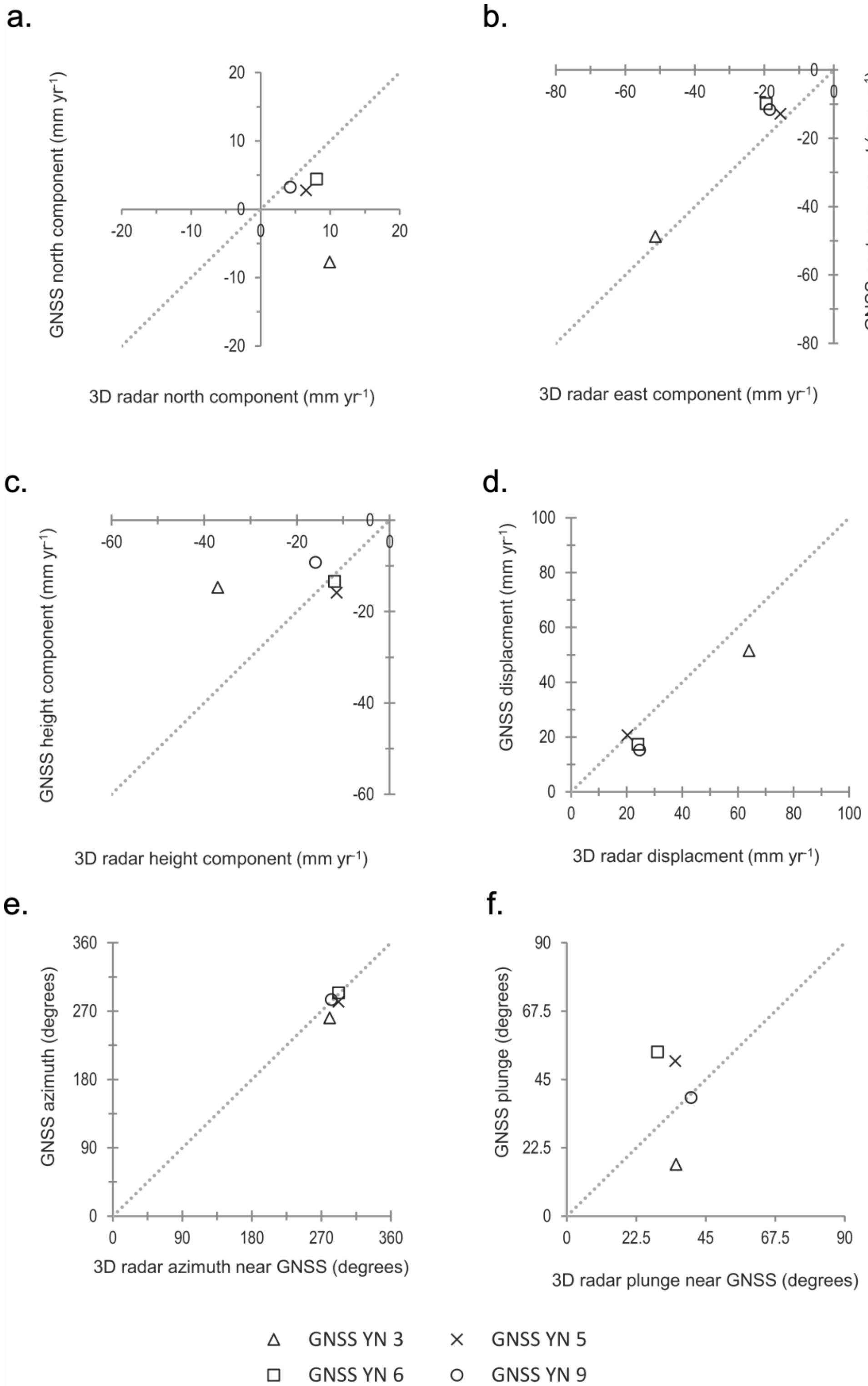

Fig. 4 – Combined 3D radar surface displacement compared to GNSS station displacement. a. North component. **b.** East component. **c.** Height component. **d.** 3D radar vector length compared to GNSS vector length. **e.** Azimuth of displacement. **f.** Plunge of displacement.

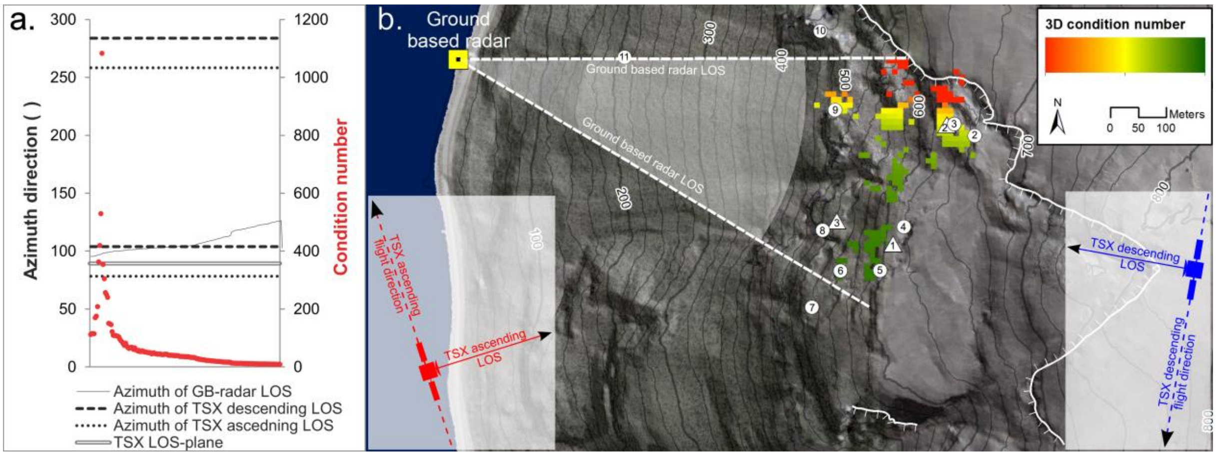

Fig. 5 – Sensitivity to displacement for 3D inversion at Jettan. a. Azimuth direction of unit vectors used in the inversion plotted with condition number. **b.** Overview of Jettan rockslide with colors representing condition number diagnosing the 3D inversion. Highest condition number means that small errors in the input data will have large consequences for the outcome of the 3D inversion. High condition numbers in a) are represented by red colors in raster. Position of ground-based radar by the fjord is marked by a yellow square and LOS-direction marked with white stippled lines. Insets show the TSX satellite LOS-directions in ascending and descending orbits. GNSS-stations are marked with circles and boreholes with triangles.

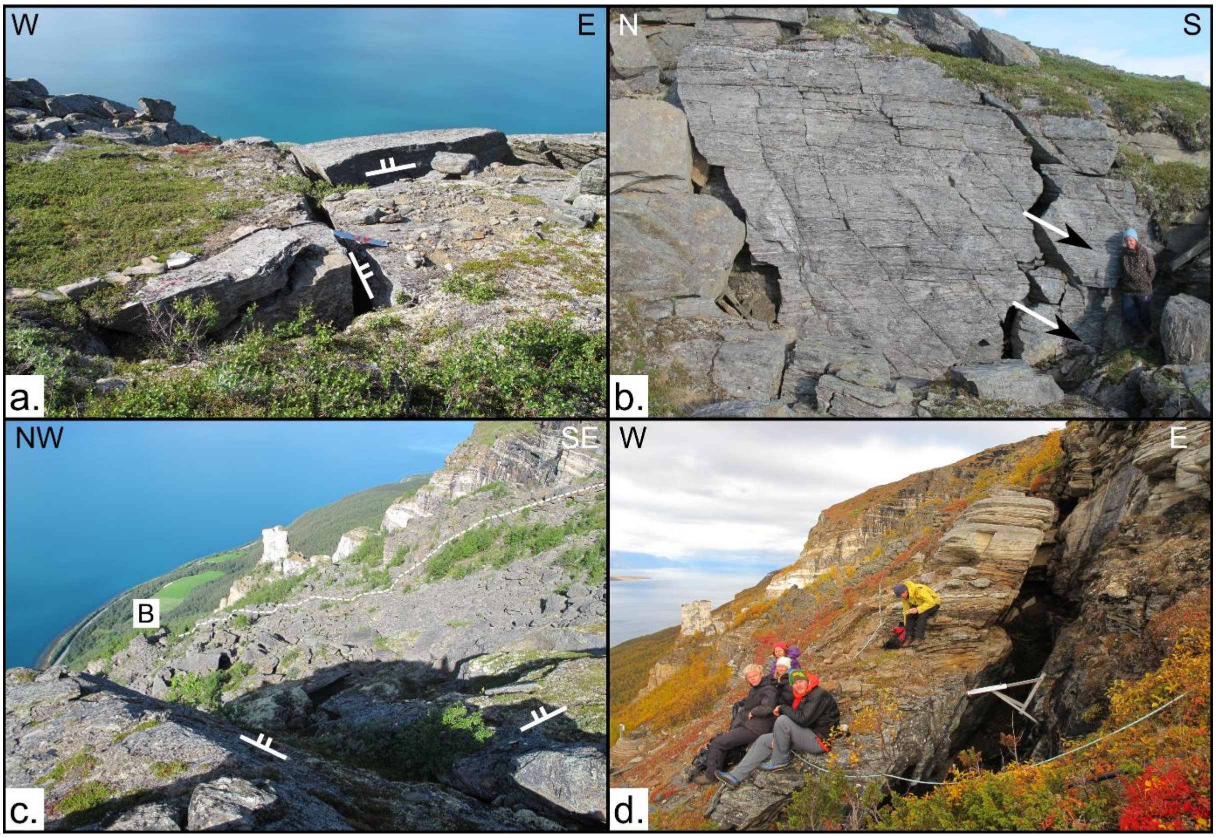

Fig. 6 – Fractures and structures in the northern and southern area. a. Smaller-scale unstable bedrock wedges in northern part of cross-section C–C' in the southern area, bounded by orthogonal fractures striking WNW-ESE and NNE-SSW, dipping NNE and NW respectively. **b.** Steep fractures curve to lower dip within meters (becomes listrics) in host rock gneisses outcropping on the steep NE-SW striking back-scarp in northern part, behind blocks in a. The outcrop shows the principle movement in a wedge-failure (Wyllie & Mah (2004), along intersection of two pre-existing fabrics, a steep NW-SE striking fracture set and a gently dipping foliation (flat fabric). Movement directions (with arrows) are recorded by open cavities between the two fabrics, notably here, with sliding along the foliation, controlled by foliation and one fracture set. **c**. Downslope view along major NW-dipping sliding surface (with tallus) bounded by orthogonal NE-dipping fracture (in front left) in the lower part of section B–B', indicating combined planar-failure movement downslope toward NW, i.e. perpendicular to fracture strike, and along intersection line between the two major fracture sets, i.e. toward WNW in upper part (right). Annotated scarp to the right are the same as pictured in Fig 2b. **d.** Close-up view of slope-parallel open fracture set in southern area (figure f), acting as sliding surface for downslope planar failures.

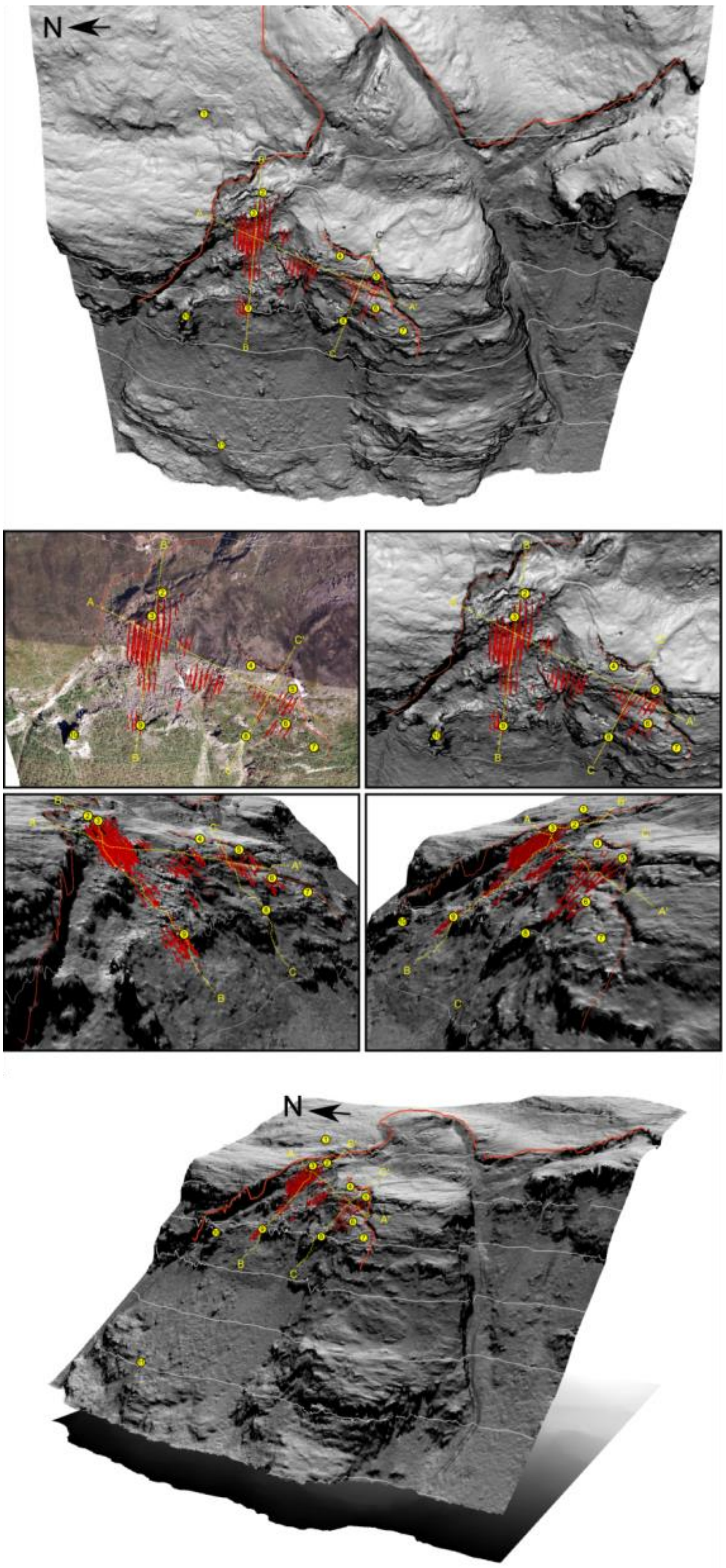

Fig. 7 – 3D displacement vectors and slope map draped on a digital elevation model (DEM) of the Jettan rockslide. Dark colors represent steep terrain, light color are flatter areas. Back scarp marked with red line. GNSS-stations marked with yellow circles and cross-

sections with stipples yellow lines. DEM and slope maps are based on 1 × 1 m resolution LIDAR data from 2014 supplied by the NMA

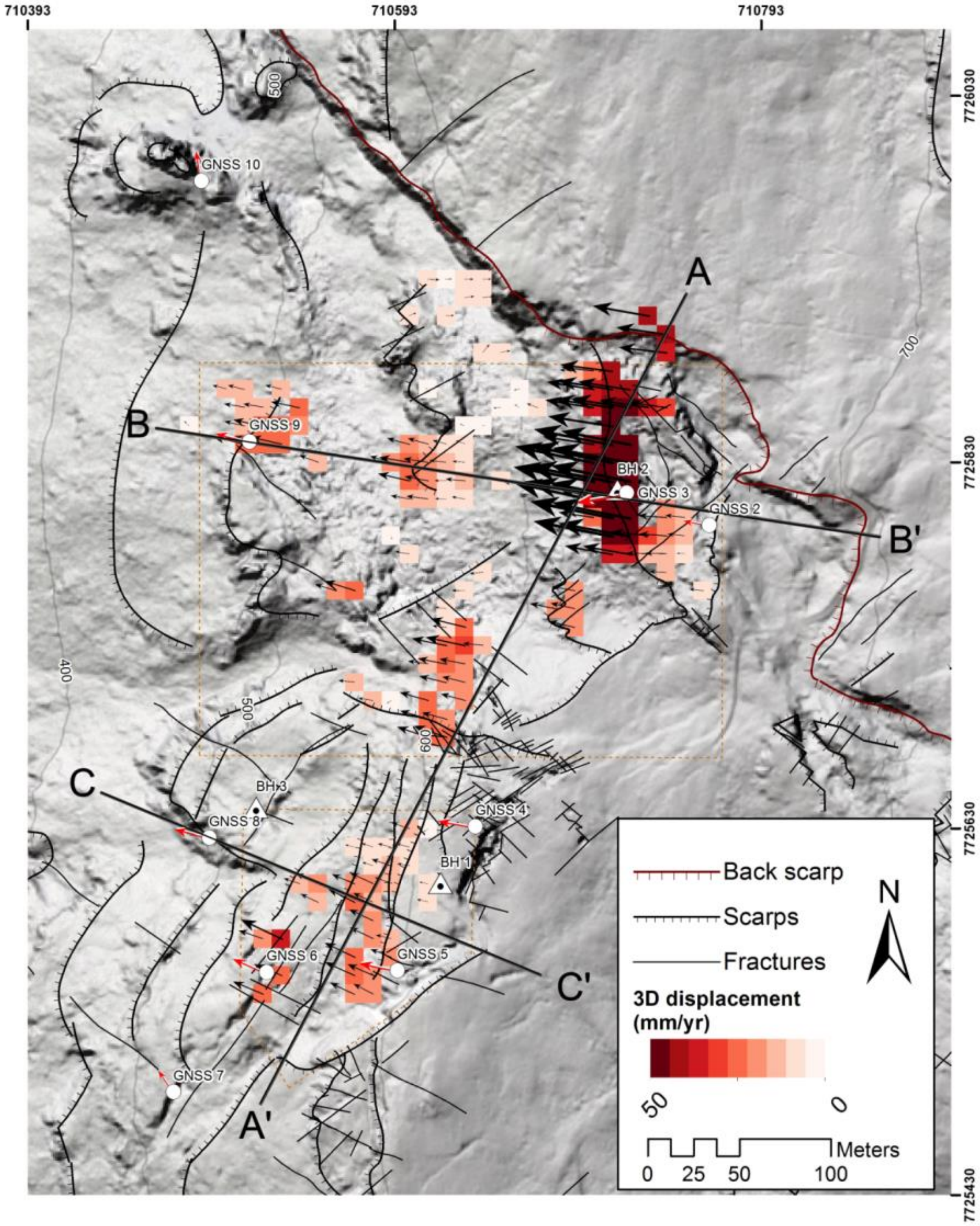

Fig. 8 – 3D displacement vectors and GNSS displacement vectors from the Jettan rockslide with geological structures (back scarp and scarps) and geomorphological elements (scarps) after Skrede (2013). Direction (azimuth) and length (mm yr^{-1}) of 3D vectors (black arrows) and GNSS vectors (red arrows) are comparable. In addition to length of black arrows the mean yearly velocity of 3D vectors is given by red to white raster. Location of cross-sections A–A', B–B' and C–C' are marked by gray solid lines. Location of borehole (BH) and GNSS stations are marked. Extent of map marked in inset in Fig. 3

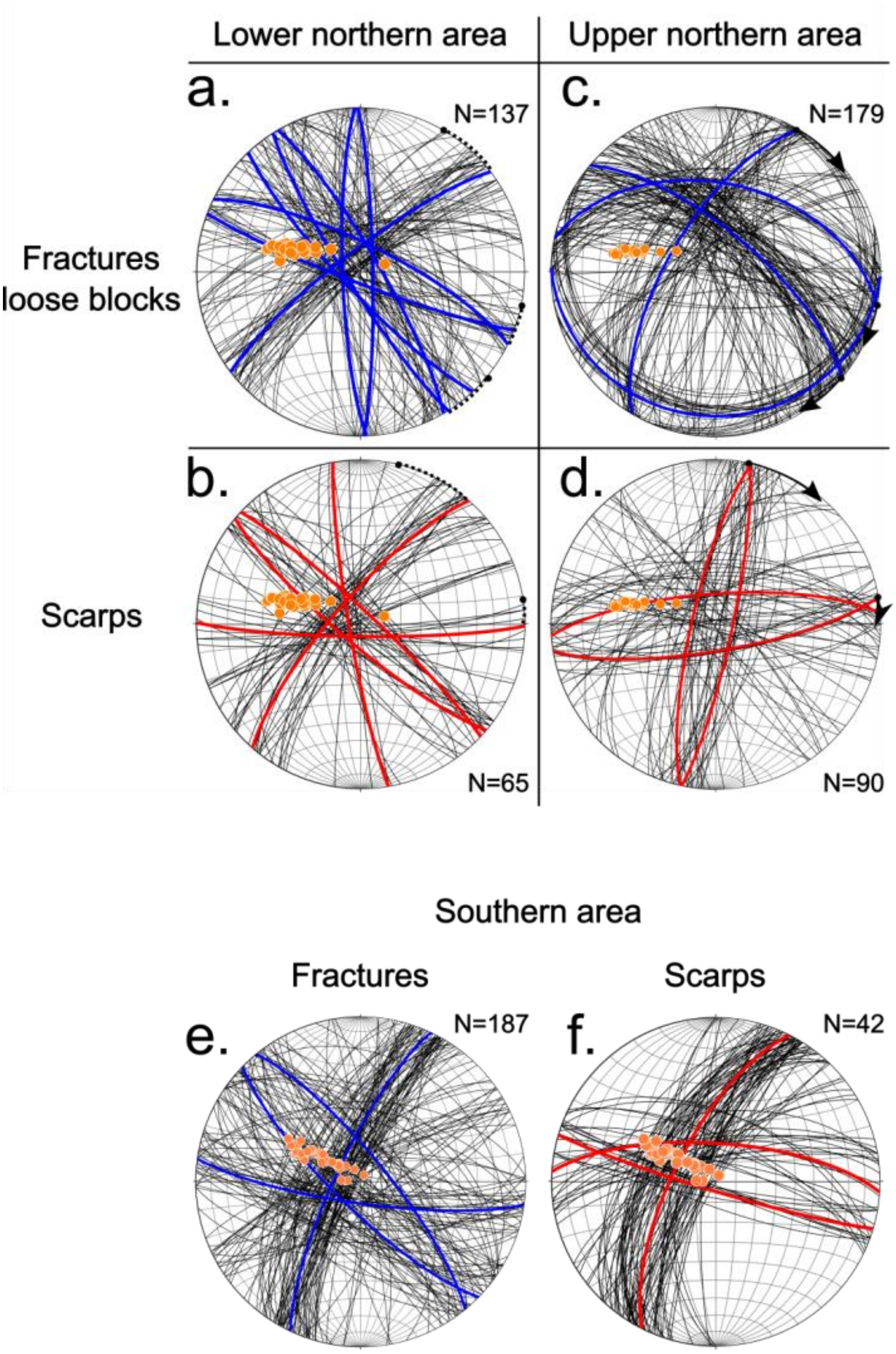

Fig. 9 – Structural data from the northern and southern area. Orientation of fractures (great circles) and 3D surface displacement vectors (orange dots) plotted in lower-hemisphere stereograms, for loose blocks and scarps in lower (**a.** and **b.**) and upper along (**c.** and **d.**) northern area along cross-section B–B', and fractures (**e.**) and scarps (**f.**) from the southern area. Individual fractures are drawn as thin black great circles, and dominant trends as thicker great circles (blue and red colors). N-values indicate number of measurements. Black arrows and stippled lines indicated difference between azimuth of structures in the upper and lower

area. Note the different trend in displacement vectors from in the northern and the southern area.

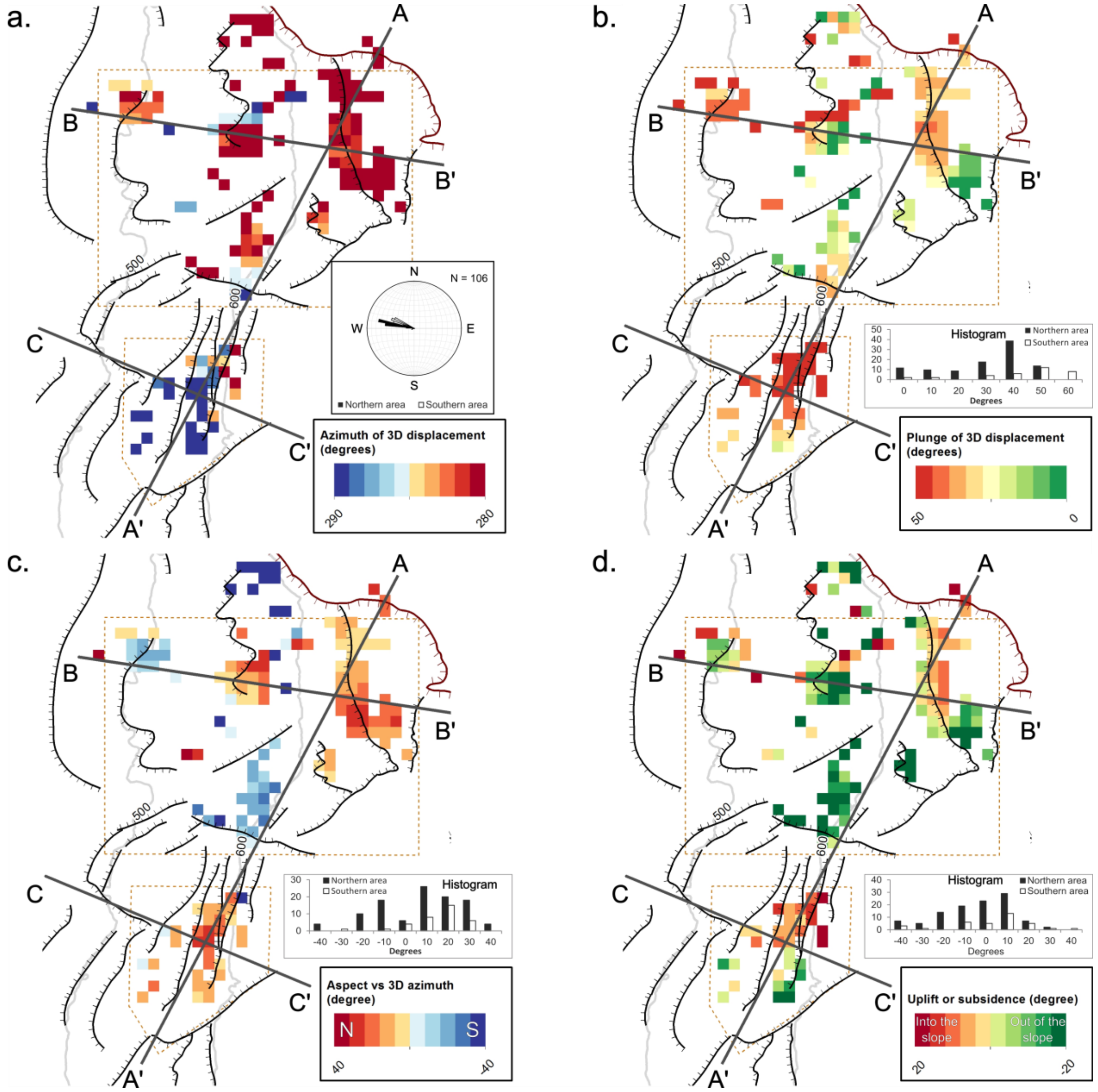

Fig. 10 – Properties of 3D displacement vectors and relation to topography and structures for the Jettan rockslide. Inset rose diagram and histograms show deviations in main azimuth and plunge trends of 3D displacement vectors in the northern and southern area of the rockslide. Extents of northern and southern area are marked with stippled lines, cross-sections A–A', B–B' and C–C' marked with dark-gray lines. **a.** Azimuth of 3D displacement vectors in degrees. **b.** Plunge of 3D displacement vectors in degrees. **c.** Difference between azimuth of 3D displacement vectors and aspect of the topography, giving aspect dependency for displacement in degrees. Positive values (red color) mean displacement more towards

north than aspect, zero mean equal azimuth direction, negative values (blue color) mean displacement more towards south than aspect. **d.** Areas with displacement into the slope (red color) and out of the slope (green color) from comparing plunge 3D displacement vector with slope of the topography. Positive values mean displacement into the slope, zero values mean equal plunge, negative values mean displacement out of the slope.

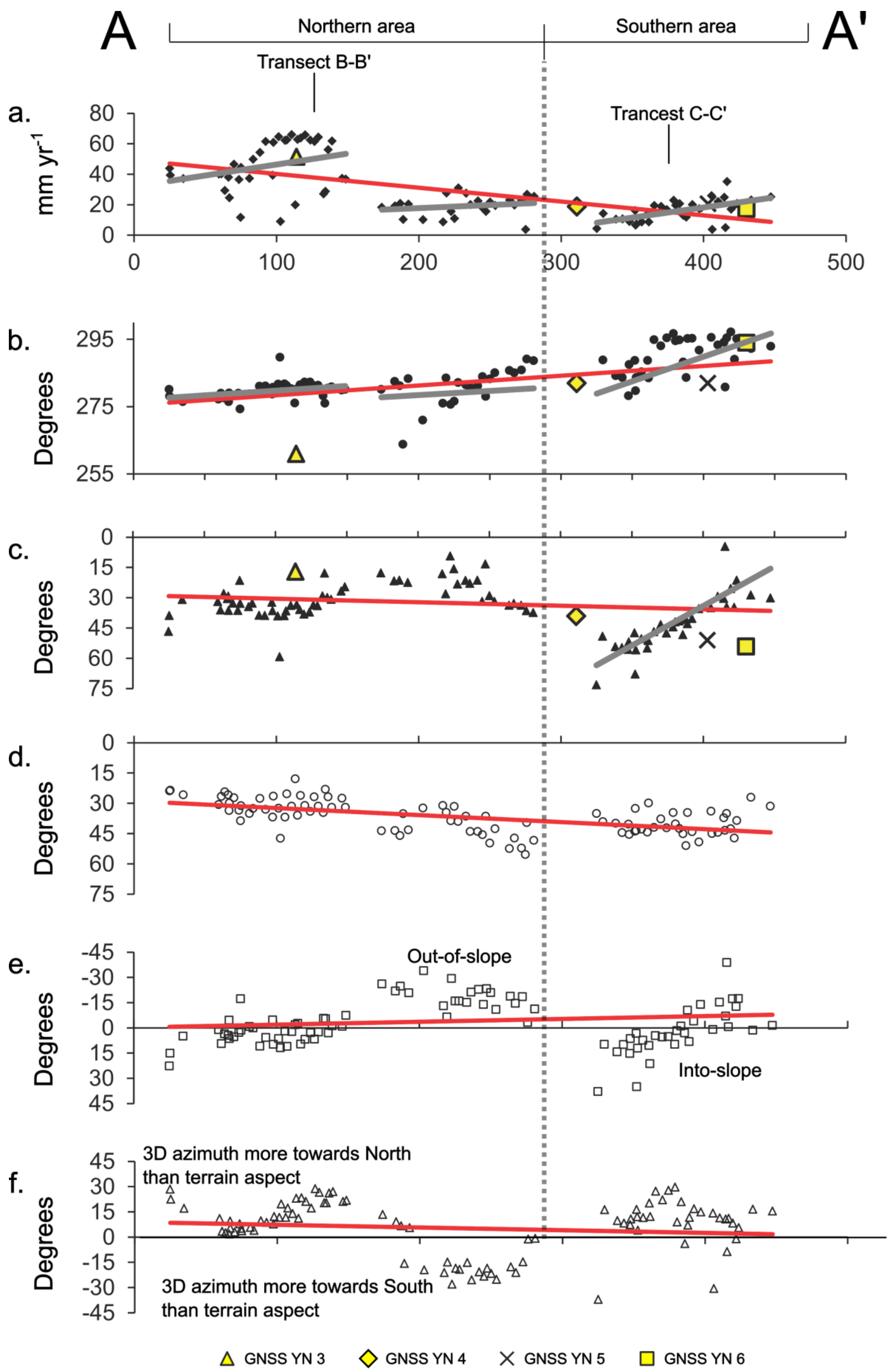

Fig. 11 – Properties of 3D vectors along cross-section A–A' and nearby GNSS-stations, including **a.** mean yearly velocity, **b.** azimuth of displacement, **c.** plunge of displacement, **d.** slope of topography, **e.** degree of uplift (slope dependency), and **f.** displacement direction towards north or south compared to aspect of topography (aspect dependency). Grey lines

indicated the linear internal trends. The boundary between the northern and the southern areas (vertical stippled line) are marked together with location of cross-sections B–B' and C–C'.

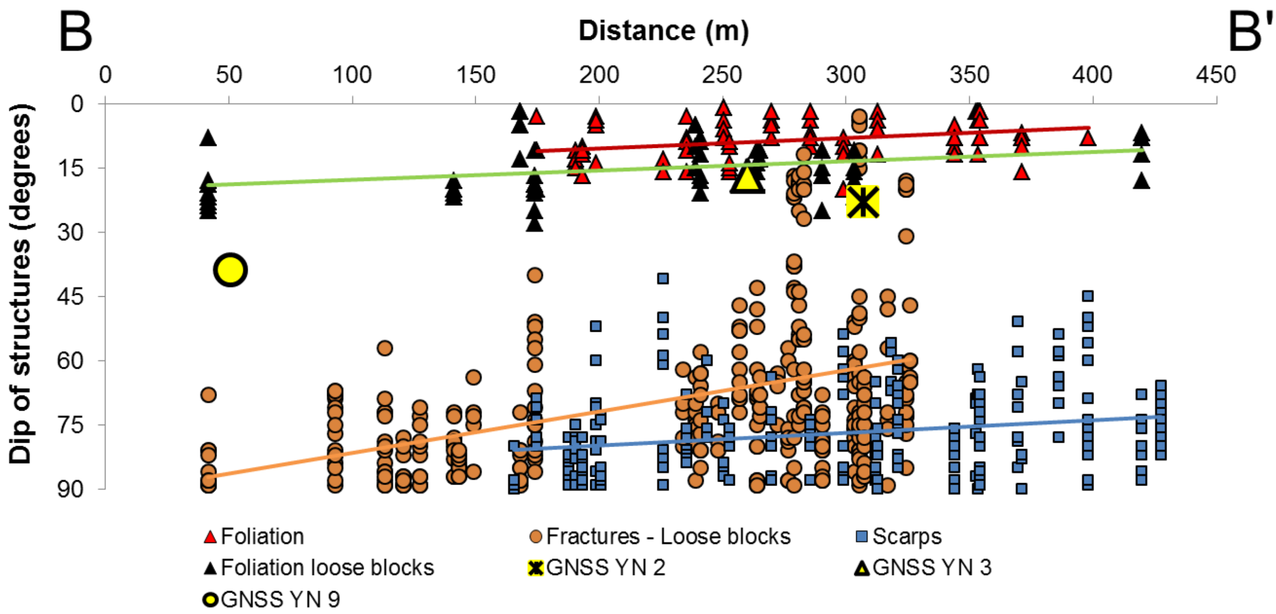

Fig. 12 – Dip of fractures, scarps and foliation mapped Skrede (2013) collected using a 320 buffer along cross-section B–B'. Mean plunge of GNSS-station from snow-free season 2009-2014) marked for GNSS stations 2, 3 and 9.

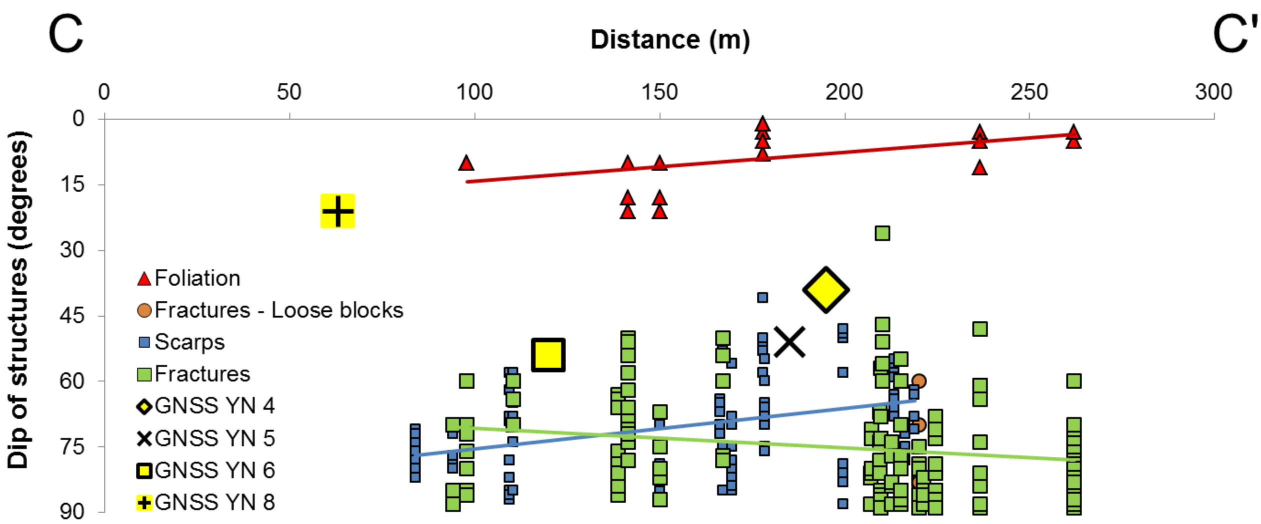

Fig. 13 – Dip of fractures, scarps and foliation mapped Skrede (2013) collected using a 320 buffer along cross-section C–C'. Mean plunge of GNSS-station from snow-free season 2009-2014) marked for GNSS station 4, 5, 6 and 8.

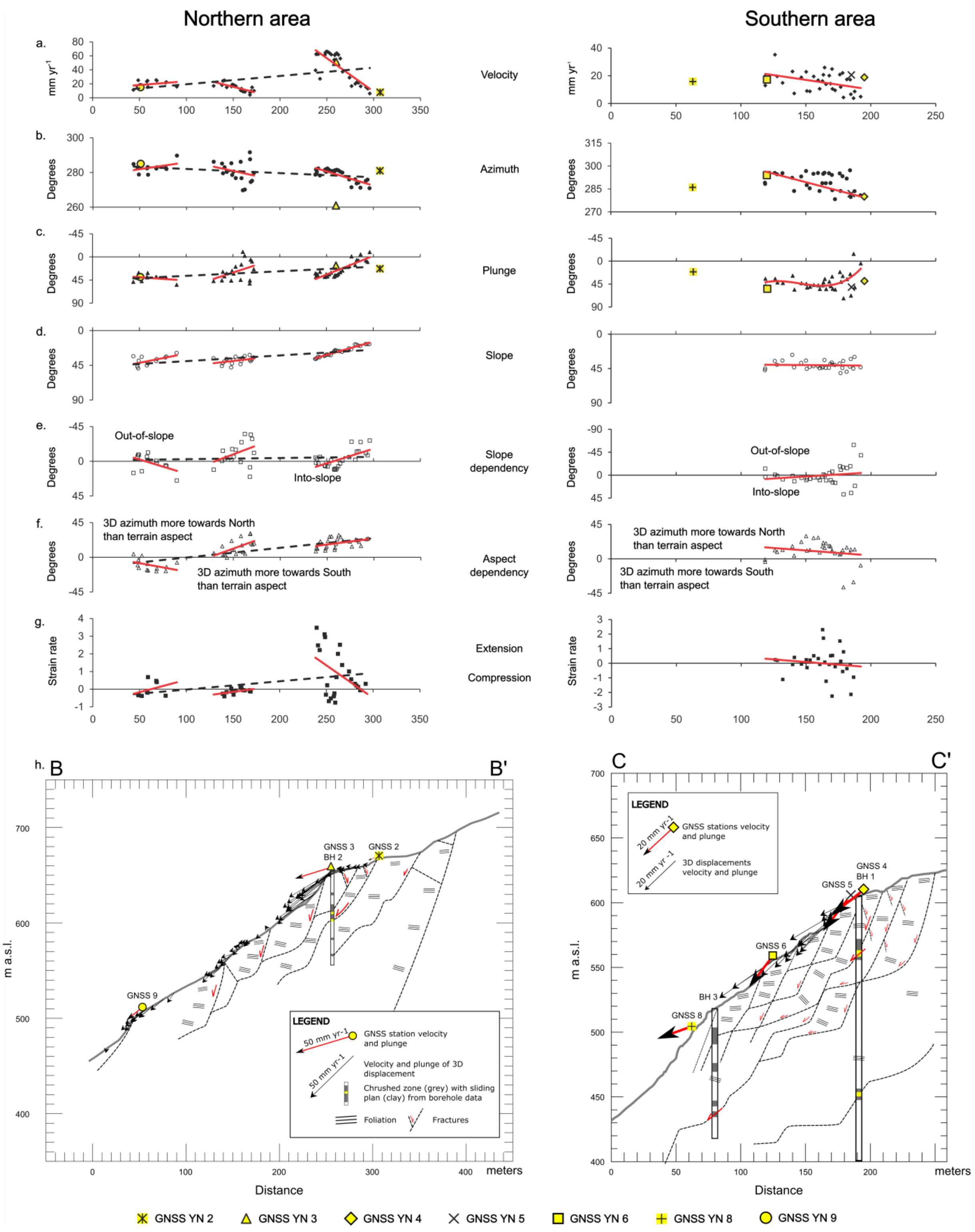

Fig. 14 **– Properties of 3D displacement and relation to topography, GNSS-stations and borehole data, along cross-sections B–B' and C–C' from the northern and southern area of the Jettan rockslide, with proposed rock slope failure models.** Three mechanisms are inferred from the cross-sections: (1) Back-rotation can be imaged as a step-wise structural pattern formed by steep NW and SE dipping fractures cut through the foliation, and/or follow more gentle dipping foliation, leading to gradually more back-rotated blocks at depth, with movement along fractures and foliation into the surface. (2) Wedge-failure collapse along planar intersection lines between NE and SW-dipping fracture sets symbolized as straight stippled lines. (3) Planar failure, also symbolized as straight stippled lines. **a.** 3D displacement velocity, **b.** azimuth and **c.** plunge. **d.** slope of topography. **e.** relation between slope of topography and plunge of displacement. **f.** relation between aspect of topography and azimuth of displacement. **g.** downslope velocity gradient (strain rate) denoting areas with compression and extension. **h.** geological cross-sections with data from DMS and core logging of boreholes (Elvebakk, 2013, 2014; Ganerød, 2013, 2014), mapped geological structures (Skrede, 2013), 3D surface displacement draped as black arrows and GNSS displacement as red arrows. All structures and displacement are projected into the trend of the cross-sections.

8 REFERENCES

Berardino, P., Costantini, M., Franceschetti, G., Iodice, A., Pietranera, L., and Rizzo, V., 2003, Use of differential SAR interferometry in monitoring and modelling large slope instability at Maratea (Basilicata, Italy): Engineering Geology, v. 68, no. 1–2, p. 31-51.

Blikra, L. H., Christiansen, H., Kristensen, L., and Lovisolo, M., 2015, Characterization, Geometry, Temporal Evolution and Controlling Mechanisms of the Jettan Rock-Slide, Northern Norway, *in* Lollino, G., Giordan, D., Crosta, G. B., Corominas, J., Azzam, R., Wasowski, J., and Sciarra, N., eds., Engineering Geology for Society and Territory - Volume 2, Springer International Publishing, p. 273-278.

Blikra, L. H., and Christiansen, H. H., 2014, A field-based model of permafrost-controlled rockslide deformation in northern Norway: Geomorphology, v. 208, p. 34-49.

Blikra, L. H., Henderson, I., and Nordvik, T., 2009, Faren for fjellskred fra Nordnesfjellet i Lyngenfjorden, Troms, NGU Rapport 2009.026, (in norwegian), p. 29.

Braathen, A., Blikra, L. H., Berg, S., and Karlsen, F., 2004, Rock-slope failures in Norway; type, geometry, deformation mechanisms and stability: Norwegian Journal of Geology, v. 84, p. 67-87.

Cavalié, O., Doin, M. P., Lasserre, C., and Briole, P., 2007, Ground motion measurement in the Lake Mead area, Nevada, by differential synthetic aperture radar interferometry time series analysis: Probing the lithosphere rheological structure: Journal of Geophysical Research: Solid Earth, v. 112, p. 18.

Chaussard, E., Wdowinski, S., Cabral-Cano, E., and Amelung, F., 2014, Land subsidence in central Mexico detected by ALOS InSAR time-series: Remote Sensing of Environment, v. 140, no. 0, p. 94-106.

Chen, C. W., and Zebker, H. A., 2001, Two-dimensional phase unwrapping with statistical models for nonlinear optimization: Proceedings of the Geoscience and Remote Sensing Symposium, 2000., v. 7, p. 3213-3215.

Elvebakk, H., 2013, Borehullslogging med optisk televiewer, Jettan 1, Nordnesfjellet, Kåfjord kommune, Troms. NGU report nr.: 2013.020, (in norwegian), p. 96.

-, 2014, Borehullslogging med optisk televiewer, Bh 2 og Bh 3, Jettan, Nordnesfjellet, Kåfjord kommune, Troms. NGU rapport nr.: 2014.016, (in norwegian), p. 119.

Eriksen, H. Ø., 2013, Slope displacement patterns observed using satellite InSAR data in the Storfjord-Kåfjord-Lyngen region, Troms, Unpublished Master Thesis, UiT-The Arctic University of Norway, Tromsø, Norway, p. 138.

Eriksen, H. Ø., Lauknes, T. R., Larsen, Y., Corner, G. D., Bergh, S. G., Dehls, J., and Kierulf, H. P., 2017, Visualizing and interpreting surface displacement patterns on unstable slopes using multi-geometry satellite SAR interferometry (2D InSAR): Remote Sensing of Environment, v. 191, p. 297-312.

Fialko, Y., Sandwell, D., Simons, M., and Rosen, P., 2005, Three-dimensional deformation caused by the Bam, Iran, earthquake and the origin of shallow slip deficit: Nature, v. 435, no. 7040, p. 295-299.

Fialko, Y., Simons, M., and Agnew, D., 2001, The complete (3-D) surface displacement field in the epicentral area of the 1999 MW7.1 Hector Mine Earthquake, California, from space geodetic observations: Geophysical Research Letters, v. 28, no. 16, p. 3063-3066.

Ganerød, G. V., 2013, Geological logging of drill core from borehole NN-01-12 at Jettan, Nordnes mountain in Troms county, Northern Norway. NGU report no. 2013.042, p. 59.

-, 2014, Geological logging of drill cores from borehole BH 02-13 and BH 03-13 at Jettan, Nordnes mountain in Troms county, Northern Norway. Ngu report no. 2014.005, p. 64.

Goldstein, R. M., Engelhardt, H., Kamb, B., and Frolich, R. M., 1993, Satellite Radar Interferometry for Monitoring Ice Sheet Motion: Application to an Antarctic Ice Stream: Science, v. 262, no. 5139, p. 1525-1530.

Goldstein, R. M., and Werner, C. L., 1998, Radar interferogram filtering for geophysical applications: Geophysical Research Letters, v. 25, no. 21, p. 4035-4038.

Gourmelen, N., Amelung, F., Casu, F., Manzo, M., and Lanari, R., 2007, Mining-related ground deformation in Crescent Valley, Nevada: Implications for sparse GPS networks: Geophysical Research Letters, v. 34, no. 9, p. L09309.

Henderson, I. H. C., Osmundsen, P. T., and Redfield, T., 2008, ROS Fjellskred i Troms: Statusrapport 2007. NGU report 2008.025, (in norwegian), p. 38.

Hernes, I., 2014, Fjellskred ved Indre Nordnes , Nordnesfjellet , Lyngen , Troms — Berggrunnens indre struktur og bevegelsesmekanismer basert på strukturell analyse og overvakingsdata, Unpublished Master Thesis, UiT-The Arctic University of Norway, Tromsø, Norway, (in norwegian), p. 136.

Husby, E. H., 2011, Fjellskred i Nomedalstinden: En strukturstyrt masseutglidning på et underliggende storskala glideplan, p. 142.

Kierulf, H. P., Steffen, H., Simpson, M. J. R., Lidberg, M., Wu, P., and Wang, H., 2014, A GPS velocity field for Fennoscandia and a consistent comparison to glacial isostatic adjustment models: Journal of Geophysical Research: Solid Earth, v. 119, no. 8, p. 6613-6629.

Kristensen, L., 2011, Ground based radar measurements at Gamanjunni 3 and Oksfjellet, Troms. Åknes/Tafjord Beredskap IKS rapport 09, (in norwegian), p. 10.

-, 2013, Bakkebasert InSAR målinger til kartlegging av bevegelse på Jettan og Indre Nordnes. Åknes/Tafjord Beredskap IKS rapport 03, (in norwegian), p. 15.

Kristensen, L., Kjølås, Å., Bergeng, T., and Rivolta, C., 2011, Ground based radar measurements at Gamanjunni 3 and Oksfjellet, Troms. Åknes/Tafjord Beredskap IKS rapport 09, (in norwegian), p. 10.

Larsen, Y., Engen, G., Lauknes, T. R., Malnes, E., and Høgda, K. A., A generic differential interferometric SAR processing system, with applications to land subsidence and snow-water equivalent retrieval (unpublished), *in* Proceedings Proc. ESA Fringe 2005, ESA ESRIN, Frascati, Italy, November 28-December 22005.

Lauknes, T. R., Shanker, A. P., Dehls, J. F., Zebker, H. A., Henderson, I. H. C., and Larsen, Y., 2010, Detailed rockslide mapping in northern Norway with small baseline and persistent scatterer interferometric SAR time series methods: Remote Sensing of Environment, v. 114, no. 9, p. 2097-2109.

Massonnet, D., Briole, P., and Arnaud, A., 1995, Deflation of Mount Etna monitored by spaceborne radar interferometry: Nature, v. 375, p. 567-570.

Nagler, T., Rott, H., Hetzenecker, M., Scharrer, K., Magnússon, E., Floricioiu, D., and Notarnicola, C., Retrieval of 3D-glacier movement by high resolution X-band SAR data, *in* Proceedings 2012 IEEE International Geoscience and Remote Sensing Symposium22-27 July 2012 2012, p. 3233-3236.

Nordvik, T., Blikra, L. H., Nyrnes, E., and Derron, M. H., 2010, Statistical analysis of seasonal displacements at the Nordnes rockslide, northern Norway: Engineering Geology, v. 114, no. 3-4, p. 228-237.

Nystad, T. M., 2014, Utvikling av geologisk modell og stabilitetsanalyse av den mest aktive delen av det ustabile fjellpartiet Jettan på Nordnesfjellet i Troms, Unpublished Master Thesis, Department of Geology and Mineral Resources Engineering, Norwegian University of Science and Technology, Trondheim, Norway, (in Norwegian), p. 180.

Peltzer, G., Crampé, F., Hensley, S., and Rosen, P., 2001, Transient strain accumulation and fault interaction in the Eastern California shear zone: Geology, v. 29, no. 11, p. 975-978.

Pieraccini, M., 2013, Monitoring of Civil Infrastructures by Interferometric Radar: A Review: The Scientific World Journal, v. 2013, p. 8.

Rasmussen, E., 2011, Fjellskred i Laksvatnfjellet, Balsfjord, Troms: indre struktur, morfologi og skredmekanismer, Unpublished Master Thesis, UiT-The Arctic University of Norway, Tromsø, Norway, (in norwegian), p. 142.

Rønning, J. S., Dalsegg, E., Heincke, B. H., Juliussen, H., and Tønnesen, J. F., 2008, Geofysiske målinger på Nordnesfjellet sommeren 2007, Kåfjord kommune, Troms, NGU Rapport nr.: 2008.024, (in norwegian), p. 33.

Skrede, I., 2013, Jettan, Nordnesfjellet, Kåfjord, Troms-indre geomtri og struktur, kinematikk og styrande faktorar av eit ustabilt fjellparti, basert på strukturellanalyse, geomorfologi og overvakingsdata, Unpublished Master Thesis, UiT-The Arctic University of Norway, Tromsø, Norway, (in norwegian), p. 176.

-, 2014, Radarkampanje ved Nordnesfjellet 2014, Norwegian Water Resources and Energy Directorate rapport 2015_40, (in norwegian), p. 22.

Strozzi, T., Wegmuller, U., Tosi, L., Bitelli, G., and Spreckels, V., 2001, Land Subsidence Monitoring with Differential SAR Interferometry: Photogrammetric Engineering & Remote Sensing, v. 67, no. 11, p. 1261-1270.

Tarchi, D., Casagli, N., Fanti, R., Leva, D. D., Luzi, G., Pasuto, A., Pieraccini, M., and Silvano, S., 2003, Landslide monitoring by using ground-based SAR interferometry: an example of application to the Tessina landslide in Italy: Engineering Geology, v. 68, no. 1–2, p. 15-30.

Tarchi, D., Rudolf, H., Luzi, G., Chiarantini, L., Coppo, P., and Sieber, A. J., SAR interferometry for structural changes detection: a demonstration test on a dam, *in* Proceedings Geoscience and Remote Sensing Symposium, 1999. IGARSS '99 Proceedings. IEEE 1999 International1999 1999, Volume 3, p. 1522-1524 vol.1523.

Tønnesen, J. F., and Dalsegg, E., 2006, Geofysiske målinger Nordnesfjellet, Kåfjord kommune. NGU rapport nr.: 2004.012, (in norwegian), p. 19.

Wyllie, D. C., and Mah, C., 2004, Rock slope engineering, CRC Press.

Zwaan, K. B., 1988, Geologisk kart over Norge. Berggrunnskart NORDREISA - M 1:250 000, (in norwegian): Norges geologiske undersøkelse.